NASA/CR—2016–219395

RotCFD Analysis of the AH-56 Cheyenne Hub Drag

Eduardo Solis
Monterey Technologies, Inc.
Ames Research Center, Moffett Field, California

Tal A. Bass
Princeton University
Ames Research Center, Moffett Field, California

Matthew D. Keith
University of Alaska Fairbanks
Ames Research Center, Moffett Field, California

Rebecca T. Oppenheim
Mississippi State University
Ames Research Center, Moffett Field, California

Bryan T. Runyon
University of Minnesota – Duluth
Ames Research Center, Moffett Field, California

Belen Veras-Alba
The Pennsylvania State University, University Park
Ames Research Center, Moffett Field, California

October 2016

NASA STI Program ... in Profile

Since its founding, NASA has been dedicated to the advancement of aeronautics and space science. The NASA scientific and technical information (STI) program plays a key part in helping NASA maintain this important role.

The NASA STI program operates under the auspices of the Agency Chief Information Officer. It collects, organizes, provides for archiving, and disseminates NASA's STI. The NASA STI program provides access to the NTRS Registered and its public interface, the NASA Technical Reports Server, thus providing one of the largest collections of aeronautical and space science STI in the world. Results are published in both non-NASA channels and by NASA in the NASA STI Report Series, which includes the following report types:

- TECHNICAL PUBLICATION. Reports of completed research or a major significant phase of research that present the results of NASA Programs and include extensive data or theoretical analysis. Includes compilations of significant scientific and technical data and information deemed to be of continuing reference value. NASA counterpart of peer-reviewed formal professional papers but has less stringent limitations on manuscript length and extent of graphic presentations.

- TECHNICAL MEMORANDUM. Scientific and technical findings that are preliminary or of specialized interest, e.g., quick release reports, working papers, and bibliographies that contain minimal annotation. Does not contain extensive analysis.

- CONTRACTOR REPORT. Scientific and technical findings by NASA-sponsored contractors and grantees.

- CONFERENCE PUBLICATION. Collected papers from scientific and technical conferences, symposia, seminars, or other meetings sponsored or co-sponsored by NASA.

- SPECIAL PUBLICATION. Scientific, technical, or historical information from NASA programs, projects, and missions, often concerned with subjects having substantial public interest.

- TECHNICAL TRANSLATION. English-language translations of foreign scientific and technical material pertinent to NASA's mission.

Specialized services also include organizing and publishing research results, distributing specialized research announcements and feeds, providing information desk and personal search support, and enabling data exchange services.

For more information about the NASA STI program, see the following:

- Access the NASA STI program home page at http://www.sti.nasa.gov

- E-mail your question to help@sti.nasa.gov

- Phone the NASA STI Information Desk at 757-864-9658

- Write to:
  NASA STI Information Desk
  Mail Stop 148
  NASA Langley Research Center
  Hampton, VA 23681-2199

NASA/CR—2016–219395

RotCFD Analysis of the AH-56 Cheyenne Hub Drag

Eduardo Solis
Monterey Technologies, Inc.
Ames Research Center, Moffett Field, California

Tal A. Bass
Princeton University
Ames Research Center, Moffett Field, California

Matthew D. Keith
University of Alaska Fairbanks
Ames Research Center, Moffett Field, California

Rebecca T. Oppenheim
Mississippi State University
Ames Research Center, Moffett Field, California

Bryan T. Runyon
University of Minnesota – Duluth
Ames Research Center, Moffett Field, California

Belen Veras-Alba
The Pennsylvania State University, University Park
Ames Research Center, Moffett Field, California

National Aeronautics and
Space Administration

Ames Research Center
Moffett Field, CA 94035-1000

October 2016

ACKNOWLEDGMENTS

A sincere thank you to our mentor, Eduardo Solis. Much of this work could not have been done without your guidance and encouragement.

Another thank you to Dr. William Warmbrodt for your enthusiasm and motivation. The Taste of California History presentations were an integral part of our work.

Thank you to Robert Vocke for always being available to answer our questions and providing us with your report and code.

Additional thanks to Adam Ewert, Alexander Grima, Ganesh Rajagopalan, Gloria Yamauchi, and Luke Novak for all of your advice and for entertaining our questions. Much of the insight we gained stemmed from your suggestions.

A final thanks to the entire Summer 2016 Simulation Group at the NASA Ames Research Center Aeromechanics Branch for making our office the best in the whole building.

Available from:

NASA STI Support Services
Mail Stop 148
NASA Langley Research Center
Hampton, VA 23681-2199
757-864-9658

National Technical Information Service
5301 Shawnee Road
Alexandria, VA 22312
webmail@ntis.gov
703-605-6000

This report is also available in electronic form at

http://ntrs.nasa.gov

TABLE OF CONTENTS

LIST OF FIGURES

LIST OF TABLES

NOMENCLATURE

A = Grid boundary cell size
a = Smallest estimated cell size in Cartesian simulation grid
D = Aerodynamic drag force
L = Aerodynamic lift force
PM = Aerodynamic pitching moment
q_c = Corrected free-stream dynamic pressure for wind tunnel conditions
q_u = Uncorrected free-stream dynamic pressure
v = Free-stream air velocity
α_c = Corrected angle of attack
α_{s} = Hub shaft angle of attack
ρ = Free-stream air density
ψ = Rotor hub azimuth angle

ABBREVIATIONS

ADD = Aviation Development Directorate
CAD = Computer-Aided Design
CFD = Computational Fluid Dynamics
CPU = Central Processing Unit
GPU = Graphics Processing Unit
RotCFD = Rotorcraft Computational Fluid Dynamics
RotUNS = Rotor Unstructured Flow Solver Application
ShapeGen = Shape Generator Software
OpenCL = Open Computing Language
CFL = Courant–Friedrichs–Lewy

ROTCFD ANALYSIS OF THE AH-56 CHEYENNE HUB DRAG

Eduardo Solis,[1] Tal A. Bass,[2] Matthew D. Keith,[3] Rebecca T. Oppenheim,[4] Bryan T. Runyon,[5]
and Belen Veras-Alba[6]

Ames Research Center

SUMMARY

In 2016, the U.S. Army Aviation Development Directorate (ADD) conducted tests in the U.S. Army 7- by 10- Foot Wind Tunnel at NASA Ames Research Center of a nonrotating 2/5th-scale AH-56 rotor hub. The objective of the tests was to determine how removing the mechanical control gyro affected the drag. Data for the lift, drag, and pitching moment were recorded for the 4-bladed rotor hub in various hardware configurations, azimuth angles, and angles of attack. Numerical simulations of a selection of the configurations and orientations were then performed, and the results were compared with the test data. To generate the simulation results, the hardware configurations were modeled using Creo and Rhinoceros 5, three-dimensional surface modeling computer-aided design (CAD) programs. The CAD model was imported into Rotorcraft Computational Fluid Dynamics (RotCFD), a computational fluid dynamics (CFD) tool used for analyzing rotor flow fields. RotCFD simulation results were compared with the experimental results of three hardware configurations at two azimuth angles, two angles of attack, and with and without wind tunnel walls. The results help validate RotCFD as a tool for analyzing low-drag rotor hub designs for advanced high-speed rotorcraft concepts. Future work will involve simulating additional hub geometries to reduce drag or tailor to other desired performance levels.

INTRODUCTION

In the late 1960s, the US Army developed strong interest in a high-speed military helicopter that was both lightweight and heavily armed. In response, Lockheed Corporation developed the AH-56 Cheyenne, which featured a novel “door hinge” for feathering of the blades and an externally mounted gyro for hub control [1]. In recent years, the Cheyenne’s unique hub design has been noted for its potential drag savings by removing the gyro and replacing it with a modern controller, which could reduce the hub drag by roughly 60 percent [2]. The U.S. Army Aviation Development Directorate (ADD) renewed interest in the improved aerodynamics of this design, and in 2016, tests were conducted in the U.S. Army 7- by 10-Foot Wind Tunnel at NASA Ames Research Center, on a 2/5th-scale AH-56 main rotor hub, to quantify the drag with and without the gyro and pitch arms [1]. Data for the lift, drag, and pitching moment were recorded for 9 different hardware configurations at varying azimuth angles and shaft angles of attack [3]. The gyro and various other parts of the hub are labeled in Figure 1.

---

[1] Monterey Technologies, Inc., 24600 Silver Cloud Ct., Monterey, California 93940.
[2] Princeton University, 1 Nassau Hall, Princeton, New Jersey 08544.
[3] University of Alaska Fairbanks, 505 South Chandalar Drive, Fairbanks, Alaska 99775.
[4] Mississippi State University, Lee Boulevard, Starkville, Mississippi 39762.
[5] University of Minnesota Duluth, 1049 University Drive, Duluth, Minnesota 55812.
[6] The Pennsylvania State University—University Park, 201 Old Main, University Park, Pennsylvania 16802.

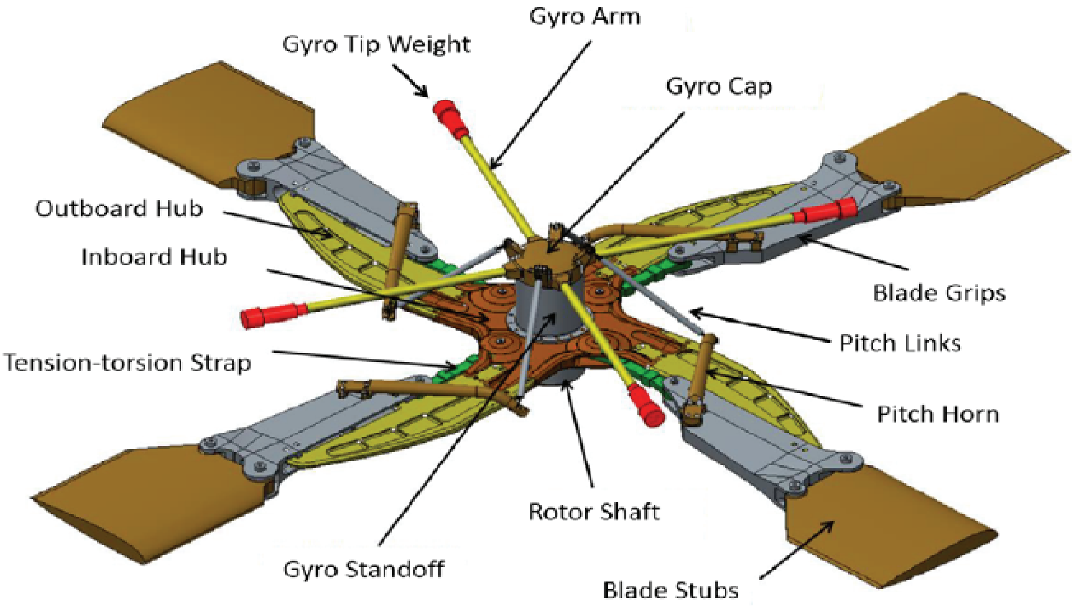

Figure 1: 3D CAD representation of the AH-56 rotor hub [3].

The goal of this work is to compare the force and moment results from the Rotorcraft Computational Fluid Dynamics (RotCFD) software package to the experimental wind tunnel data. RotCFD was used to simulate the rotor hub in both wind tunnel and free-stream conditions to predict lift, drag, and pitching moment. Drag was of greatest interest as the hub is a low-drag design. The simulations conducted in free-stream conditions were compared with wind tunnel data that was corrected to quantify hub performance in such conditions. In addition, simulations conducted in wind tunnel conditions were compared with uncorrected experimental data with the aim of validating the CFD software as an accurate tool in predicting hub performance. This would allow further configurations to be evaluated using RotCFD instead of wind tunnel testing.

ROTORCRAFT COMPUTATIONAL FLUID DYNAMICS

RotCFD is a software package for the simulation of rotorcraft flows developed by Sukra Helitek, in collaboration with NASA and the U.S. Army. It is a mid-fidelity CFD software that features an integrated design environment with tools to create simple geometries, generate grids, and simulate fluid flow using multiple flow solver applications. The use of RotCFD for this project contributed to generating feedback for the developer and debugging the code.

Rotor Unstructured Flow Solver Application (RotUNS) is an incompressible, unsteady, and unstructured Navier–Stokes flow solver in RotCFD. RotUNS was chosen to run all of the simulations for its ability to capture geometries with a higher fidelity than the other structured flow solvers available. While unstructured grids generally take more computational time than structured ones, the increase in geometry fidelity was necessary to capture the complex hub configurations to a certain accuracy.

HUB CONFIGURATIONS

Due to time limitations, only 4 of the 10 configurations tested in the wind tunnel were simulated in RotCFD. These configurations were modeled in Creo Parametric and imported into Rhinoceros 5, both of which are three-dimensional CAD modeling software programs. The geometries were simplified by removing bolts, gaps, and cavities, and then exported as an STL file format. The Shape Generator (ShapeGen) software in RotCFD was used to achieve more compact geometry files. Figure 2 shows a comparison of the initial geometry in Creo Parametric and the simplified geometry in Rhino.

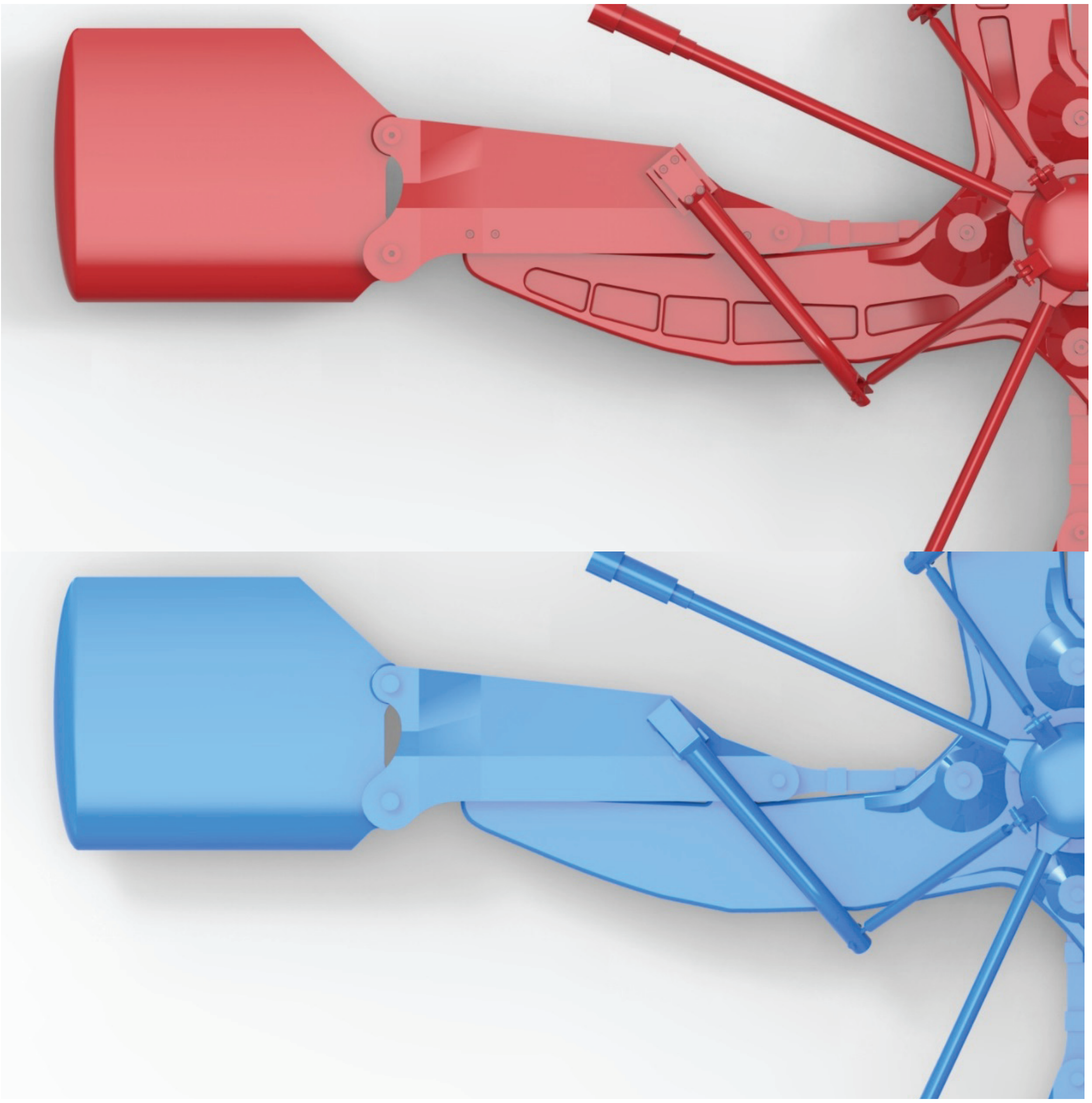

Figure 2: A comparison of the initial geometry modeled in Creo Parametric (top) and simplified geometry modeled in Rhinoceros 5 (bottom).

The first rotor hub configuration tested, known as Configuration 4, was the fixed section of the hub without the control system and is shown in Figure 3. Configuration 6, which featured the complete hub geometry as it was on the Cheyenne, was then tested; an illustration of the hub is shown in Figure 4. Configuration 8 is a version of Configuration 4, with added aerodynamic fairing; Configuration 8 is shown in Figure 5. The test stand alone, Configuration 0 as shown in Figure 6, was simulated in RotCFD in hopes of validating the software's ability to match the wind tunnel conditions. The nine configurations that were tested in the wind tunnel are shown in Appendix A.

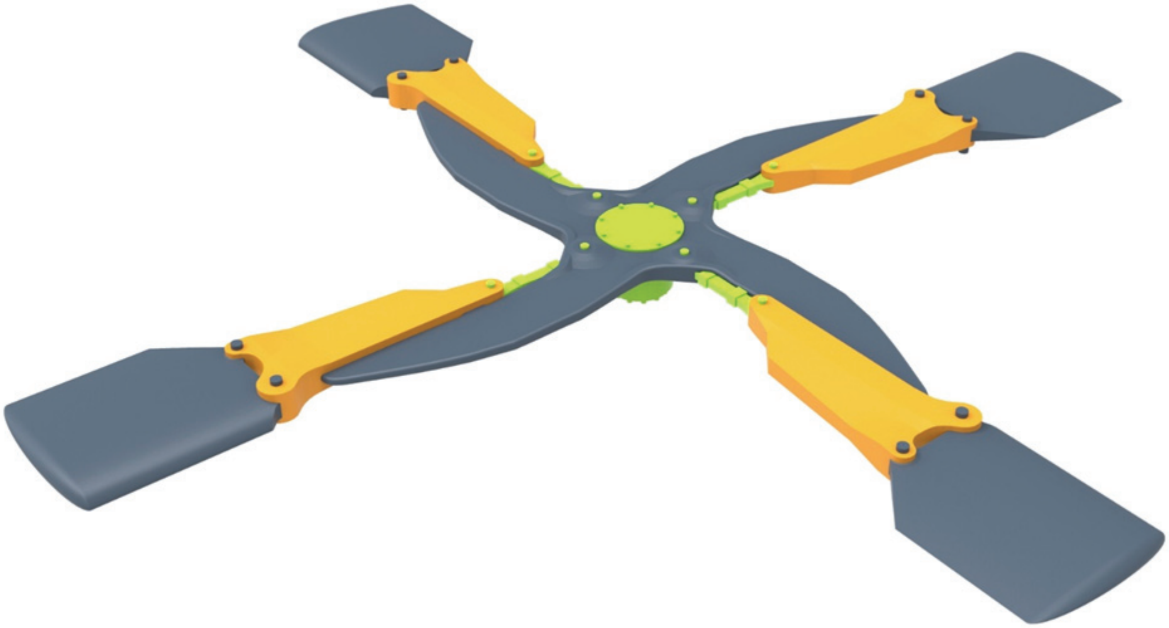

Figure 3: Configuration 4—Fixed hub and blade stubs.

Figure 4: Configuration 6—Configuration 4 with pitch horns and control gyro (blue).

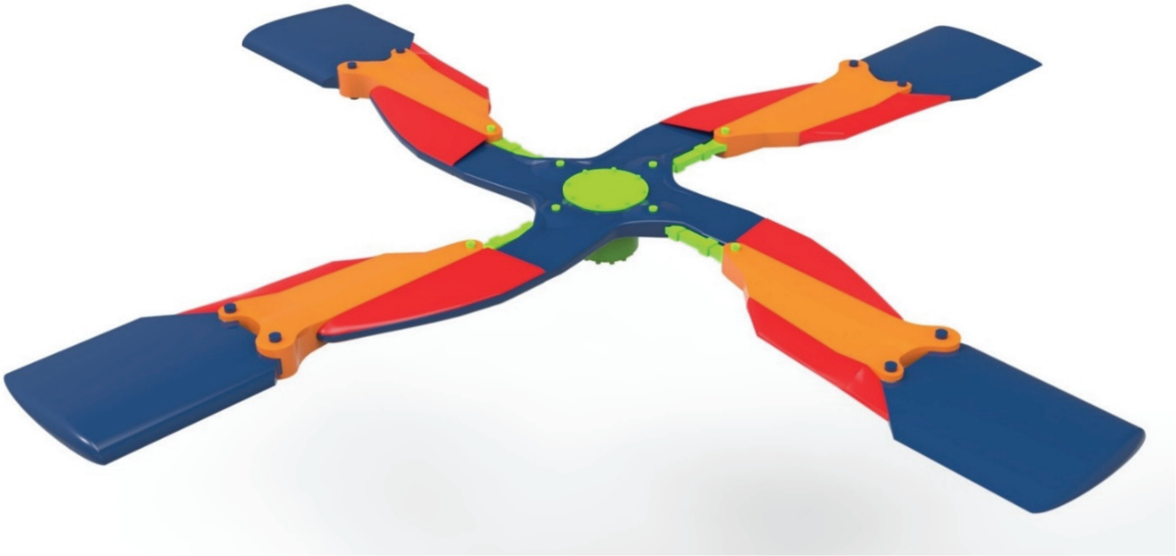

Figure 5: Configuration 8—Configuration 4 with aerodynamic fairings (red).

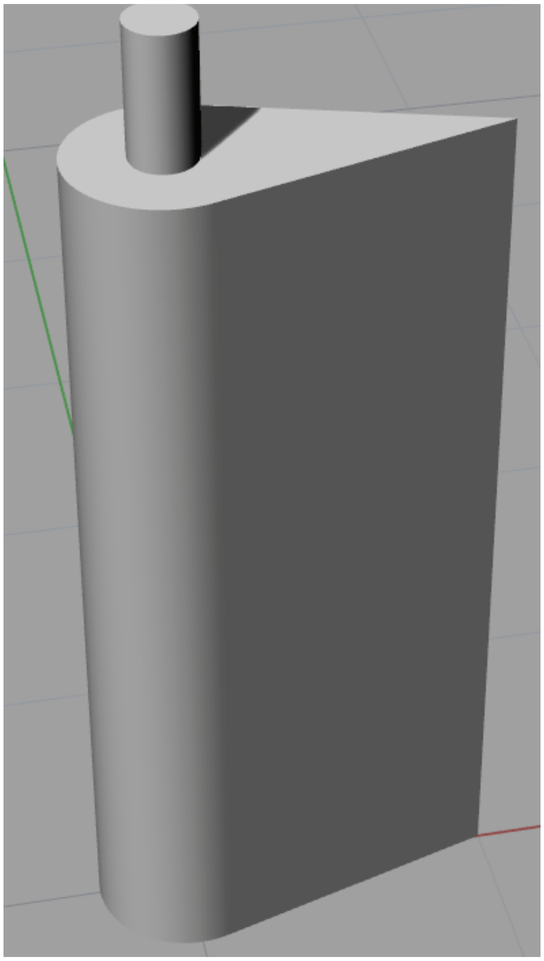

Figure 6: 3D CAD representation of Configuration 0.

Configurations 4, 6, and 8 were simulated at azimuth angle $\psi = 0°$ and $45°$ and shaft angle of attack $\alpha_s = 0° \text{ and } 6°$. A depiction of the hub angles and dimensions is shown in Figure 7. The combination of configurations and angles resulted in a total of 12 cases that were simulated. Because each of these cases were simulated in both wind tunnel and free-stream conditions, a total of 24 cases were run (excluding Configuration 0). A test matrix containing all of the RotCFD simulations run is shown in Table 1.

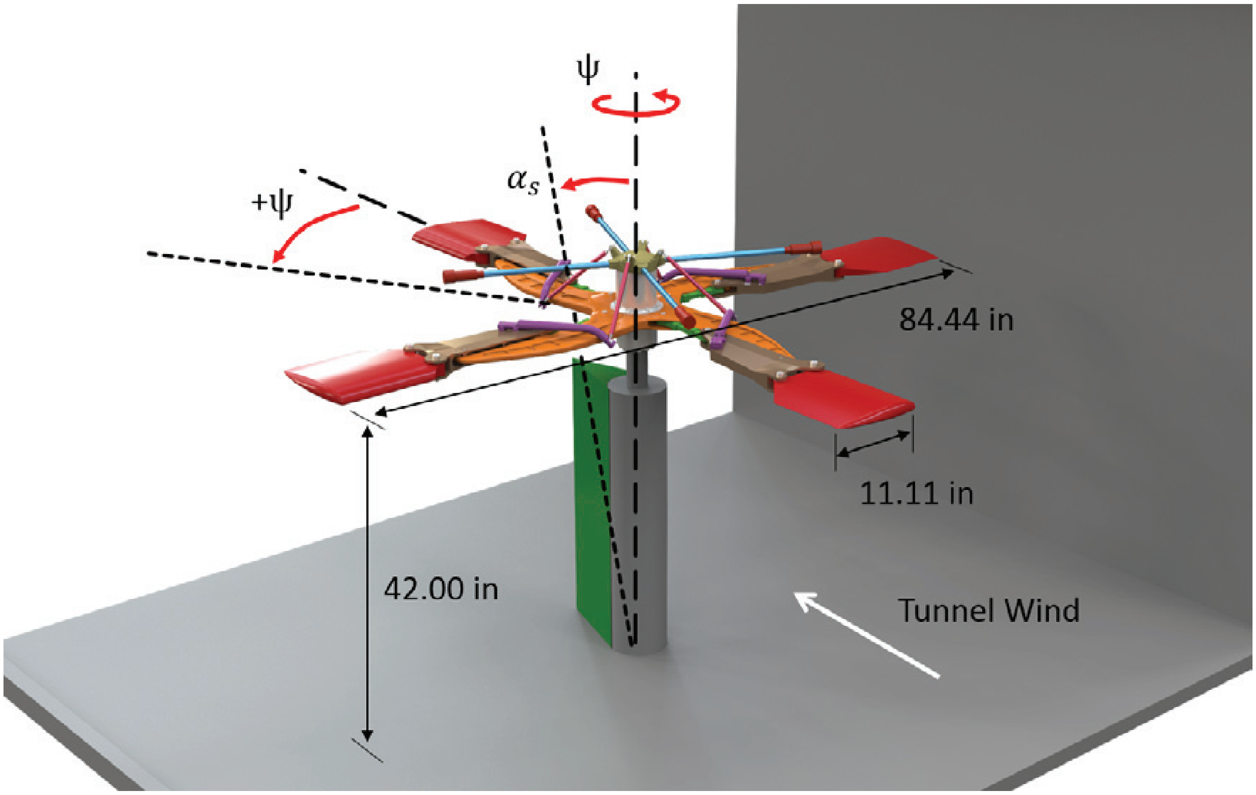

Figure 7: 3D CAD representation of the hub in the 7- by 10-foot wind tunnel with labeled angles and dimensions [3].

Table 1: Test case matrix for the RotCFD simulations studied.

Test Configuration	Azimuth Angle	Shaft Angle	Test Condition
Configuration 0	0	0	Wind Tunnel
Configuration 4	0	0	Wind Tunnel
			Free Stream
		6	Wind Tunnel
			Free Stream
	45	0	Wind Tunnel
			Free Stream
		6	Wind Tunnel
			Free Stream
Configuration 6	0	0	Wind Tunnel
			Free Stream
		6	Wind Tunnel
			Free Stream
	45	0	Wind Tunnel
			Free Stream
		6	Wind Tunnel
			Free Stream
Configuration 8	0	0	Wind Tunnel
			Free Stream
		6	Wind Tunnel
			Free Stream
	45	0	Wind Tunnel
			Free Stream
		6	Wind Tunnel
			Free Stream

SIMULATION CONDITIONS

Nearly all of the simulations were run on graphics processing units (GPUs) as opposed to central processing units (CPUs). This new feature in RotCFD allows run times to be decreased through the use of Open Computing Language. The geometries were imported into RotCFD, and the configuration orientations were set in RotUNS along with the flow properties provided in Table 2. The simulations used a realizable k-epsilon turbulence model featured in RotUNS.

Table 2: Simulation flow properties.

Flow Property	Value
Static Density $\left[\frac{slg}{ft^3}\right]$	0.002377
Static Temperature $[^\circ R]$	518.69
Gas Constant $\left[\frac{ft-lb}{slg-^\circ R}\right]$	1718
Specific Heat Ratio	1.4
Dynamic Viscosity $\left[\frac{slg}{ft-s}\right]$	3.74E-07
Static Pressure $\frac{lb}{ft^2}$	2118.17

Free-Stream Simulation Conditions

Cases that simulated free-stream conditions were run with a velocity of 230 ft/s in the x-direction. In such cases, the domain was restricted to a 10-ft cube that encompassed the hub, where all of the walls of the domain were set to have a velocity of 230 ft/s in the x-direction and 0 ft/s in the y- and z-directions. The number of boundary cells was set to 10 for each direction generating 1-ft^3 base cells. The most important aspect of gridding is the level of refinement. Refinement is based on the boundary cells, which are the largest. Equation 1 was used to estimate the smallest Cartesian cell size, where n is the level of refinement.

$$a = \frac{A}{2^{n-1}} \tag{1}$$

A refinement level of four was applied to the entire region. Refinement boxes were placed around the entirety of the geometry with a level of six as shown in Figure 8, and the geometry was body-fitted to create tetrahedral cells near the object surface with a refinement level of 6. Figure *9* shows the grid surrounding one of the hub arms. More examples of the grids used are shown in Appendix A.

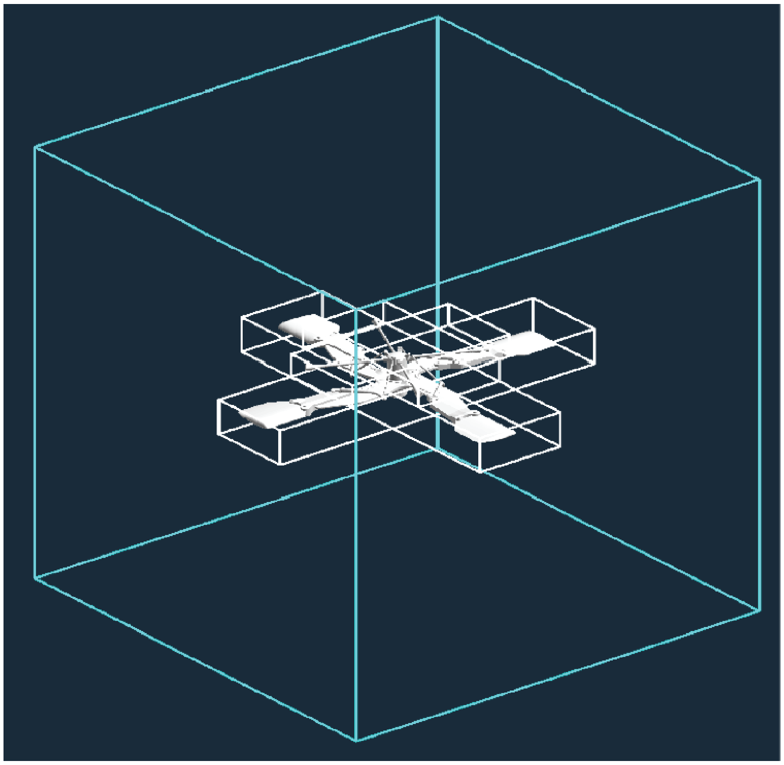

Figure 8: Computational domain as shown in RotCFD, including the rotor hub and refinement boxes.

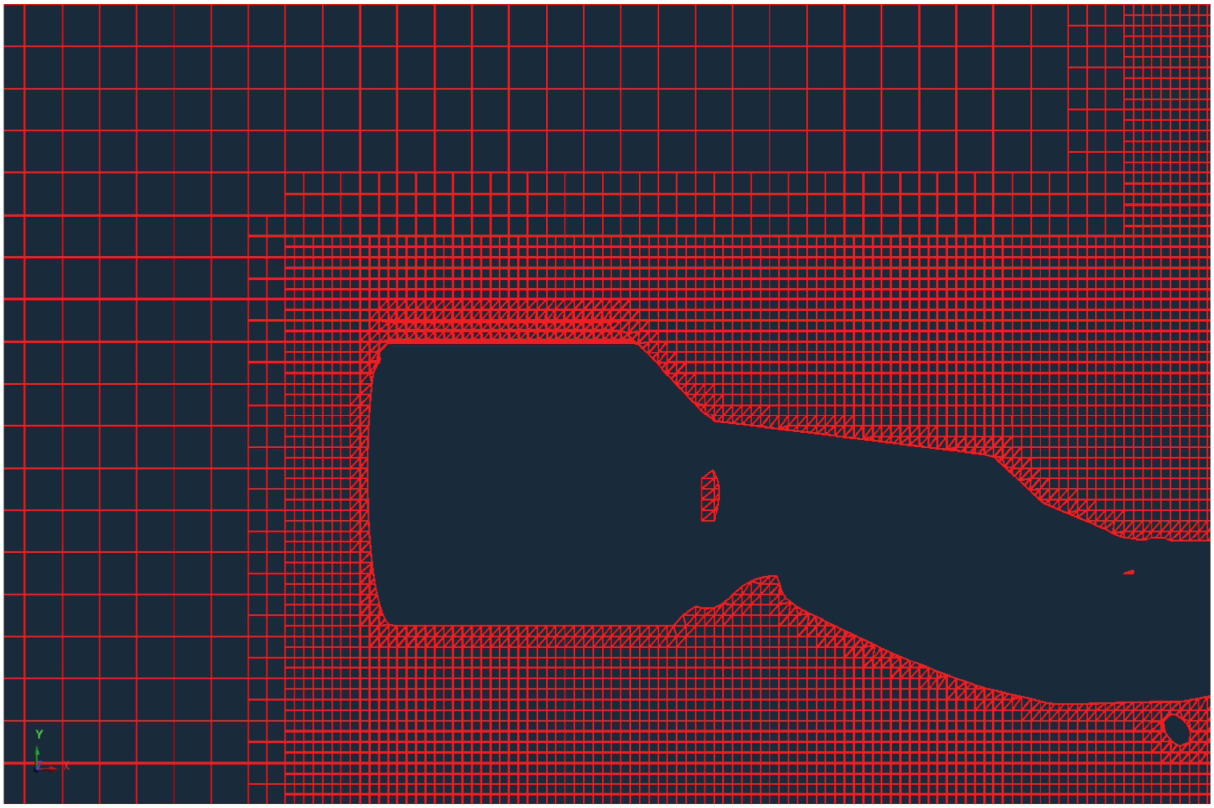

Figure 9: RotCFD display of the grid surrounding one of the arms.

Total simulation time is determined by the amount of time it takes a plane of particles at one boundary to travel to the opposite boundary. Simulations conducted in free-stream conditions were modeled for a minimum of 0.05 seconds to allow the flow to completely pass through the domain. A fine spatial grid must be accompanied by a fine time grid to create a simulation that will converge on the correct solution; if particles skip cells, the simulation will diverge. The condition below, in Equation 2, was used to calculate an appropriate time step size, Δt, based on the estimated minimum cell length, Δx; the 1 on the right-hand side represents the Courant–Friedrichs–Lewy (CFL) number. A smaller CFL number should be used for cases employing body-fitted grids; however, the number should be as close to 1 as possible in order to limit simulation time. Total time steps for a simulation run of 0.05 seconds ranged from 5,000 to 30,000.

$$v \cdot \frac{\Delta t}{\Delta x} < 1 \tag{2}$$

Wind Tunnel Simulation Conditions

Cases that simulated wind tunnel conditions were run with the recorded wind tunnel velocity for each particular case; these velocities ranged from 225–230 ft/s. In such cases, the domain was restricted to a 7-ft x 10-ft x 15-ft box, which reflects the dimensions of the wind tunnel test section used. The cell sizes were the same as those for the free-stream condition. The boundary condition was set to viscous walls (no-slip condition). Simulations modeling wind tunnel conditions also included the wind tunnel test stand. These simulations were modeled for a minimum of 0.065 seconds to allow air particles to fully pass through the domain. Total time steps ranged from 6,500 to 16,000. Configuration 0 was also run under these conditions. Tables regarding the tests performed and their conditions are shown in Appendix B.

RESULTS

RotCFD results were compared to the data collected during wind tunnel testing of the hub in the 7- by 10-Foot Wind Tunnel. Results were required to be within 10 percent of the drag value reported by the experimental results. A secondary requirement was to be within 10 percent of the lift value, with some exception, as explained in Simulation Conditions. Values were taken only from converged solutions, which means the residuals and force and moment trends must have reached an asymptote. An example of the force-moment diagram for a converged case is shown in Figure 10.

The results from the RotCFD simulations, and their comparisons with the wind tunnel data, are shown in Table 3. In order to correct for conditions within the wind tunnel, aerodynamic tares were applied to the results; the corrected results are shown in Table 4. More information on the aerodynamic tares applied are shown in Appendix B. Specific information regarding the time and spatial gridding for the corrected and uncorrected results is shown in Appendices C and D, respectively.

A few trends can be seen in the results presented in Table 3. For example, a value of 230 ft/s was used for all cases that simulated free-stream conditions. This resulted in dynamic pressures that were 1–3 percent higher than the corrected wind tunnel dynamic pressures. Cases that simulated wind tunnel conditions used velocities taken directly from the wind tunnel data.

Another apparent trend is seen in cases with $\psi = 0°$. These cases produced more accurate drag results when compared to the wind tunnel data. In contrast, cases with a shaft angle of 6° tend to have more accurate results in both lift and pitching moment data.

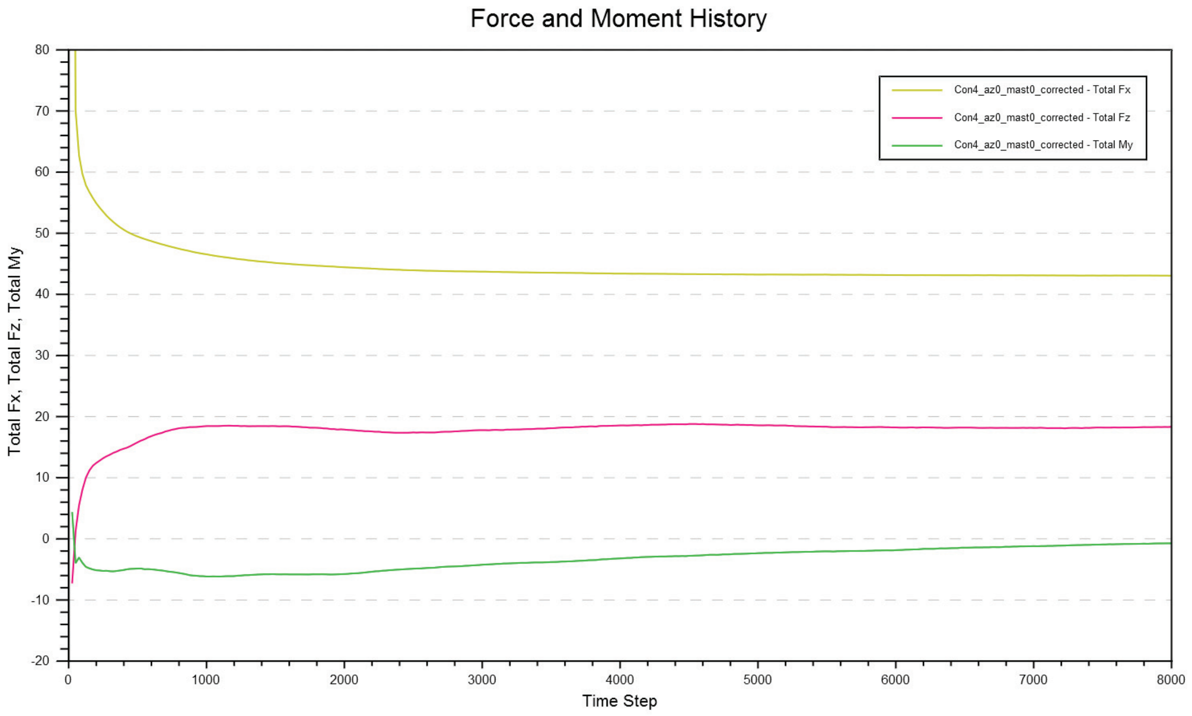

Figure 10: Force and moment history of Configuration 4 at $\psi = 0^\circ$ and $\alpha_s = 0^\circ$ modeled in free-stream conditions.

Table 3: RotCFD results compared to 7- by 10-foot wind tunnel test data.

Configuration and Orientation					7 x 10 Cases				RotCFD Cases				Error			
Flow Velocity (ft/s)	Configuration	Wall Condition	Azimuth Angle (deg)	Mast Angle (deg)	q (lb/ft^2)	Drag (lb)	Lift (lb)	Moment (ft-lb)	q (lb/ft^2)	Drag (lb)	Lift (lb)	Moment (ft-lb)	q (%)	Drag (%)	Lift (%)	Moment (%)
225.4	4	Uncorrected	0	0	60.36	43.13	36.13	–51.37	60.36	44.82	26.78	6.30	0.00	+3.92	–25.88	–112.3
225.3	4	Uncorrected	0	6	60.35	61.48	113.35	–21.55	60.35	57.27	114.17	36.83	0.00	–6.85	+0.72	–158.5
225.0	4	Uncorrected	45	0	59.98	39.71	26.01	–34.95	59.98	40.56	11.05	24.86	0.00	+2.14	–57.52	–171.1
226.1	4	Uncorrected	45	6	60.34	58.05	167.90	30.61					0.00			
230.0	4	Corrected	0	0	61.54	43.10	21.80	10.40	62.87	43.05	18.34	–0.74	+2.16	–0.12	–0.16	–107.0
230.0	4	Corrected	0	6	61.78	61.80	99.10	46.50	62.87	56.06	114.20	41.53	+1.76	–9.28	+15.24	–10.69
230.0	4	Corrected	45	0	61.09	39.70	11.70	26.90	62.87	38.84	3.05	10.72	+2.91	–2.17	–73.95	–60.16
230.0	4	Corrected	45	6	61.87	58.70	153.60	98.50	62.87	52.60	125.02	84.98	+1.62	–10.39	–18.61	–13.73
226.6	6	Uncorrected	0	0	60.08	75.01	18.51	–51.35					0.00			
226.2	6	Uncorrected	0	6	59.86	90.20	101.61	–17.01					0.00			
226.9	6	Uncorrected	45	0	60.00	71.44	13.35	–50.69					0.00			
228.9	6	Uncorrected	45	6	60.88	88.92	152.60	35.58					0.00			
230.0	6	Corrected	0	0	61.54	75.10	4.30	10.50	62.87	72.51	–4.89	7.12	+2.16	–3.45	–187.93	–32.19
230.0	6	Corrected	0	6	61.51	90.50	87.30	50.90	62.87	86.72	90.67	49.33	+2.21	–4.18	+3.86	–3.08
230.0	6	Corrected	45	0	61.38	71.40	–1.00	11.10	62.87	77.47	–22.74	4.83	+2.42	+8.51	–2174.23	–56.45
230.0	6	Corrected	45	6	62.70	89.40	138.30	103.60	62.87	87.68	97.15	82.22	–0.27	–1.93	–29.76	–20.64
227.1	8	Uncorrected	0	0	60.20	33.01	56.92	–47.25	60.20	38.08	28.15	7.01	0.00	+15.36	–50.54	+115.4
228.7	8	Uncorrected	0	6	60.91	50.62	159.50	2.58					0.00			
228.5	8	Uncorrected	45	0	60.27	32.63	39.84	–38.58					0.00			
230.4	8	Uncorrected	45	6	61.15	49.36	185.92	27.71					0.00			
230.0	8	Corrected	0	0	61.38	33.10	42.60	14.60	62.87	35.98	19.26	1.39	+2.48	+8.70	–54.79	–90.48
230.0	8	Corrected	0	6	62.37	51.20	145.20	70.60	62.87	50.46	128.00	44.98	+0.80	–1.46	–11.85	–36.29
230.0	8	Corrected	45	0	61.40	32.70	25.60	23.20	62.87	35.31	7.87	15.45	+2.39	+7.98	–69.26	–33.41
230.0	8	Corrected	45	6	62.71	50.20	171.60	95.70	62.87							

Table 4: Data with aero tares applied (used for comparison with RotCFD cases under wind tunnel conditions).

Configuration	Wall Condition	Azimuth Angle (deg)	Mast Angle (deg)	$\alpha_{s,u}$ (deg)	Drag Tare (lb)	Lift Tare (lb)	Moment Tare (ft-lb)	Drag with Aero Tare (lb)	Lift with Aero Tare (lb)	Moment with Aero Tare (ft-lb)
4	Uncorrected	0	0	–0.02	48.67	13.27	–54.33	43.13	36.13	–51.37
4	Uncorrected	0	6	6.01	54.92	24.95	–59.35	61.48	113.35	–21.55
4	Uncorrected	45	0	0.012	48.69	13.29	–54.35	39.71	26.01	–34.95
4	Uncorrected	45	6	5.976	54.85	24.80	–59.31	58.05	167.90	30.61
6	Uncorrected	0	0	0.01	48.69	13.29	–54.35	75.01	18.51	–51.35
6	Uncorrected	0	6	5.951	54.80	24.69	–59.29	90.20	101.61	–17.01
6	Uncorrected	45	0	–0.048	48.66	13.25	–54.31	71.44	13.35	–50.69
6	Uncorrected	45	6	6.042	54.98	25.10	–59.38	88.92	152.60	35.58
8	Uncorrected	0	0	0.005	48.69	13.28	–54.35	33.01	56.92	–47.25
8	Uncorrected	0	6	6.043	54.98	25.10	–59.38	50.62	159.50	2.58
8	Uncorrected	45	0	–0.033	48.67	13.26	–54.32	32.63	39.84	–38.58
8	Uncorrected	45	6	5.971	54.84	24.78	–59.31	49.36	185.92	27.71

DISCUSSION

Figure 11 is a plot of D/q vs. azimuth angle (ψ) [3]; this figure summarizes data taken during testing in the 7- by 10-foot wind tunnel. Each color represents a configuration over the range of azimuth angles tested. The downward pointing triangles are data points for $\alpha = 6°$, while the upward pointing triangles are data points for $\alpha = 0°$. Figure 12 shows the summarized RotCFD results overlaid on Figure 11 for direct comparison of the RotCFD results to the wind tunnel data. Triangles outlined in black represent RotCFD results for each successful case; the level of accuracy varies. Comparing the drag over dynamic pressure between the two studies is a better comparison than comparing force results directly. Normalizing the drag force against dynamic pressure is a more comparable metric because it eliminates the differences in drag due to differing flow velocities.

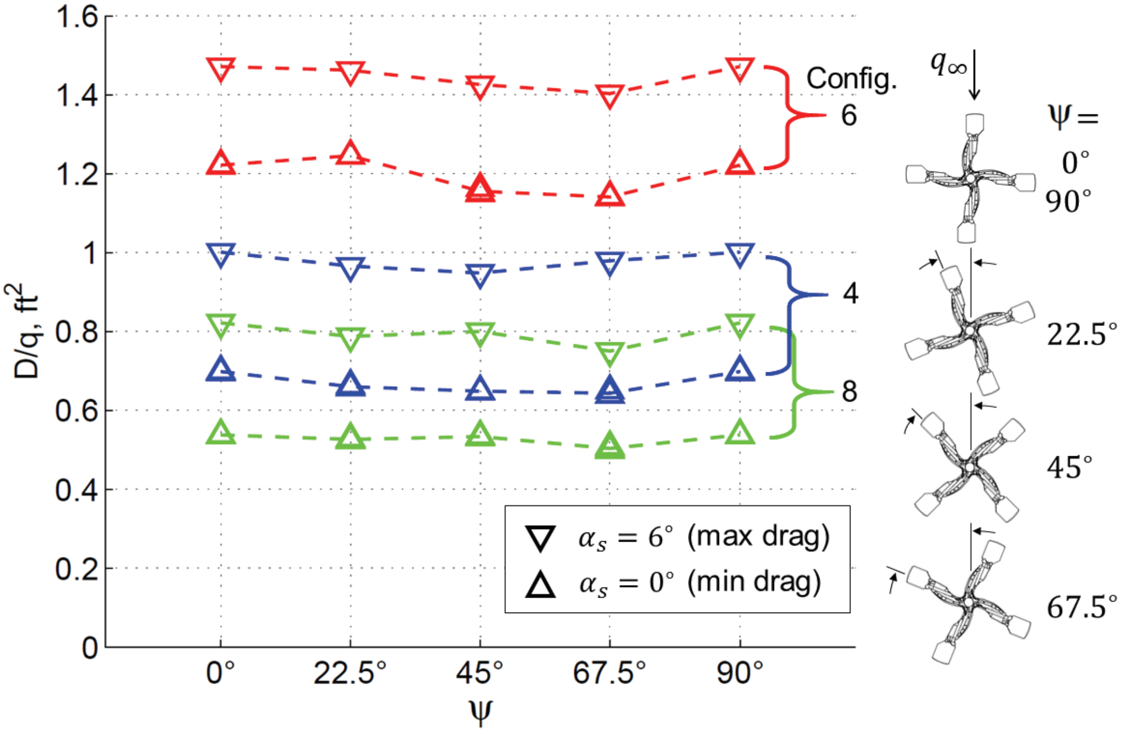

Figure 11: Plot of D/q vs. azimuth angle for wind tunnel data [3].

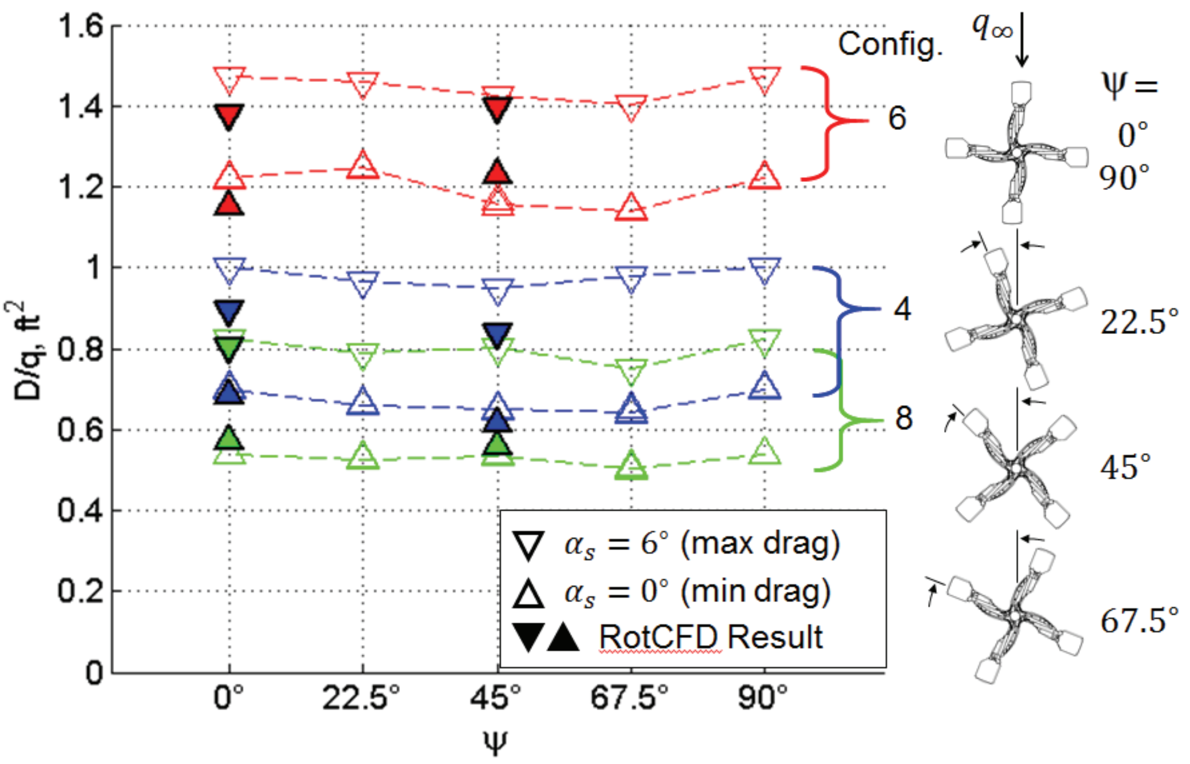

Figure 12: Plot of D/q vs. azimuth angle with RotCFD results overlaid on wind tunnel data.

Many of the initial cases had issues converging. The time grid was chosen according to the Δt calculated using Equation 2. Prior reports have suggested using a value of 0.5 instead of 0.9 for grids with tetrahedral cells [4]. Equation 2 was used to calculate a Δt of 5.43×10^{-5}s. The resulting time grid attempted for cases using free-stream conditions is shown in Table 5. Although the time grid for these cases was carefully calculated, any case where the geometry was rotated to a nonzero angle initially diverged. The number of time steps was then increased iteratively until the cases converged.

Table 5: Original calculated time grid.

Time Length	**Time Steps**	**Iterations**
0.05	5,000	10

In order to approximate the geometry in RotCFD, the software develops a grid based on the model; an example of how the gridding process in RotCFD works is shown in Figure 13. The tetrahedral grid is laid on top of the model and points of intersection are found. The nearest grid nodes and edges are then distorted slightly in order to linearize the curved surfaces of the model. This process results in a large number of tetrahedra that approximate the surface [5].

While this gridding method does a sufficient job of approximating the model, it can also create unexpectedly small cells, which change the necessary resolution of the time grid. In Figure 14, a close-up is shown of one of the control gyro arms with an exceptionally small cell. These smaller cells pose an issue, as it is more likely for the flow to skip over these cells and cause the solver to diverge. It was determined that the time grid should be adjusted to prevent these cells from being skipped.

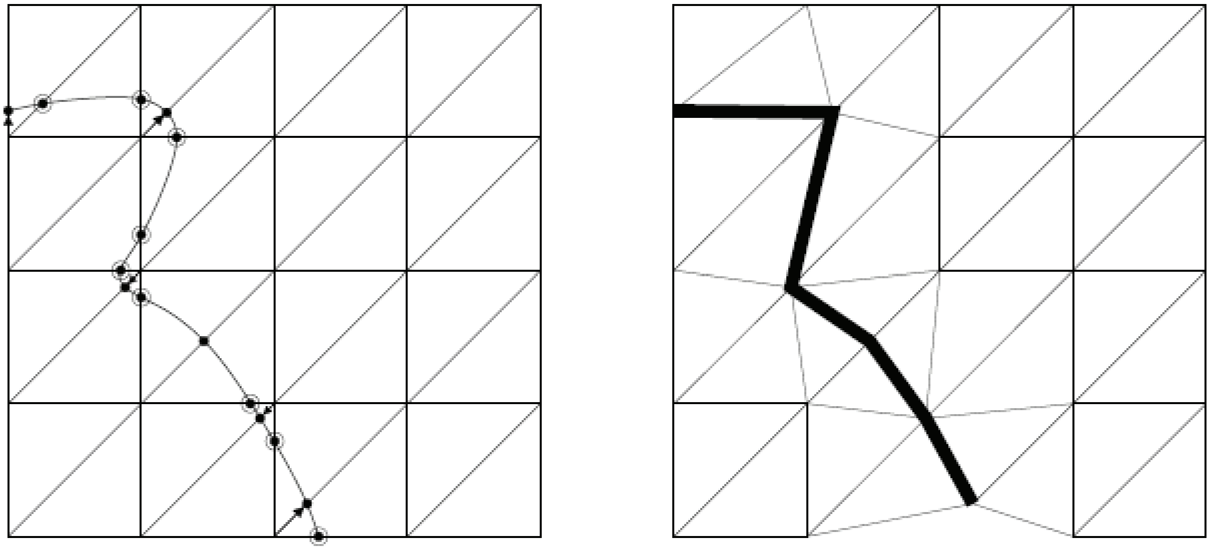

Figure 13: Example of RotCFD grid generation method with a 2D geometry [4].

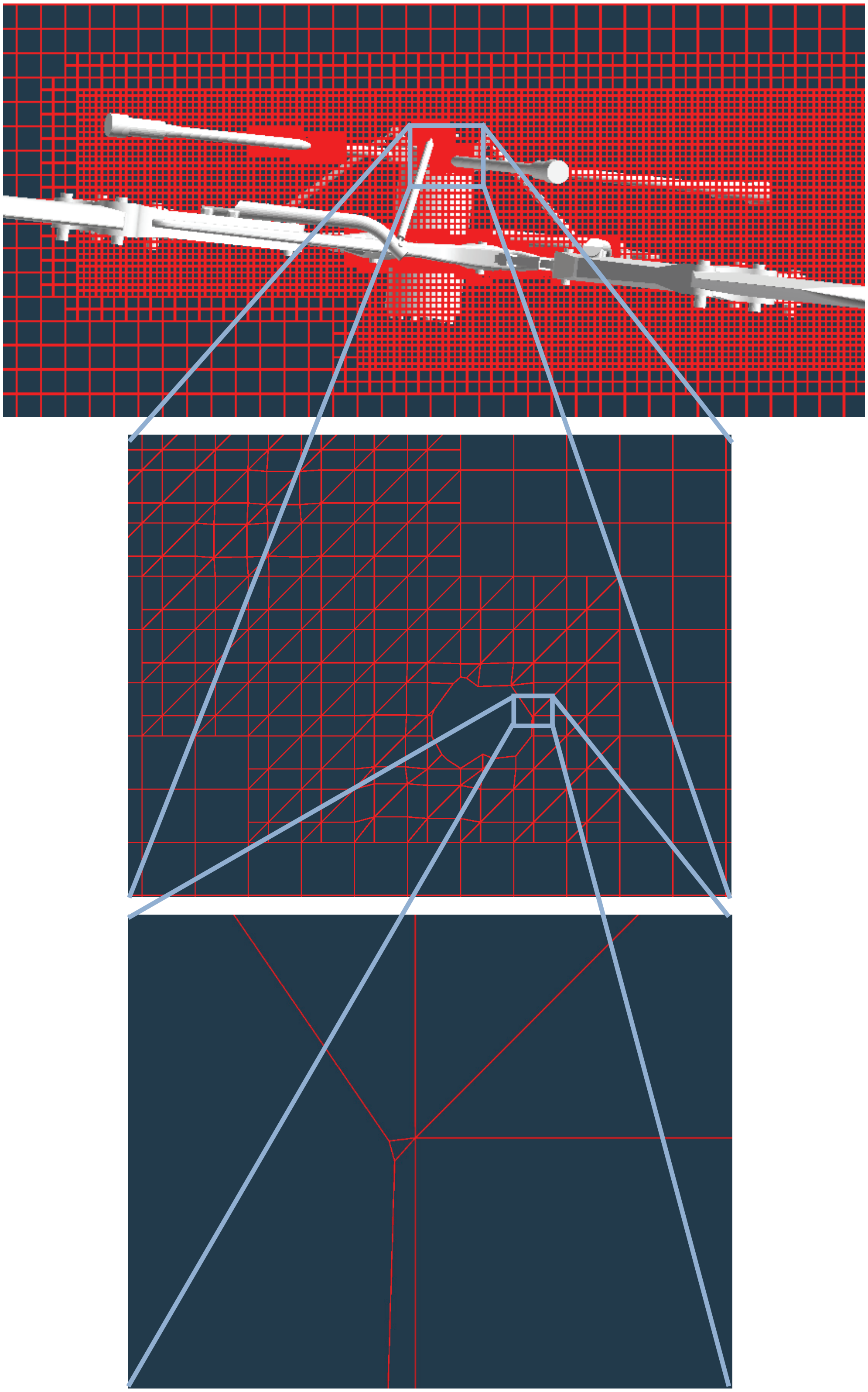

Figure 14: Close-up of small and irregular cell-shape that could lead to diverging solutions.

A result of this grid generation process was that rotating the body tended to produce unexpectedly small cells. This phenomenon is specific to the geometry, as rotating the hub caused a greater number of intersections between the body and the cells due to the nature of the geometry and Cartesian grid. Figure 15 illustrates the grid differences between objects aligned and nonaligned with the Cartesian grid. One possible solution to this challenge was to rotate the flow directions instead of the geometry, as the grid does not have to regenerate for these cases [5]. This solution was not possible for the cases that simulated wind tunnel conditions as the computational domain boundaries served as the wind tunnel walls. Rotating the flow in these cases would have altered the wind tunnel effects. It was possible to rotate the flow in the cases that simulated free-stream conditions to decrease the likelihood of divergence. However, RotCFD has been documented to produce different results depending on the rotation of the geometry or flow direction. It was therefore decided that only the geometry should be rotated for all of the cases to ensure consistency.

As a result of the changing grid, the Δt had to be decreased further from the initial calculations. A CFL value of 0.05 or smaller is suggested to achieve convergence with cases that have a complex geometries and highly refined grids.

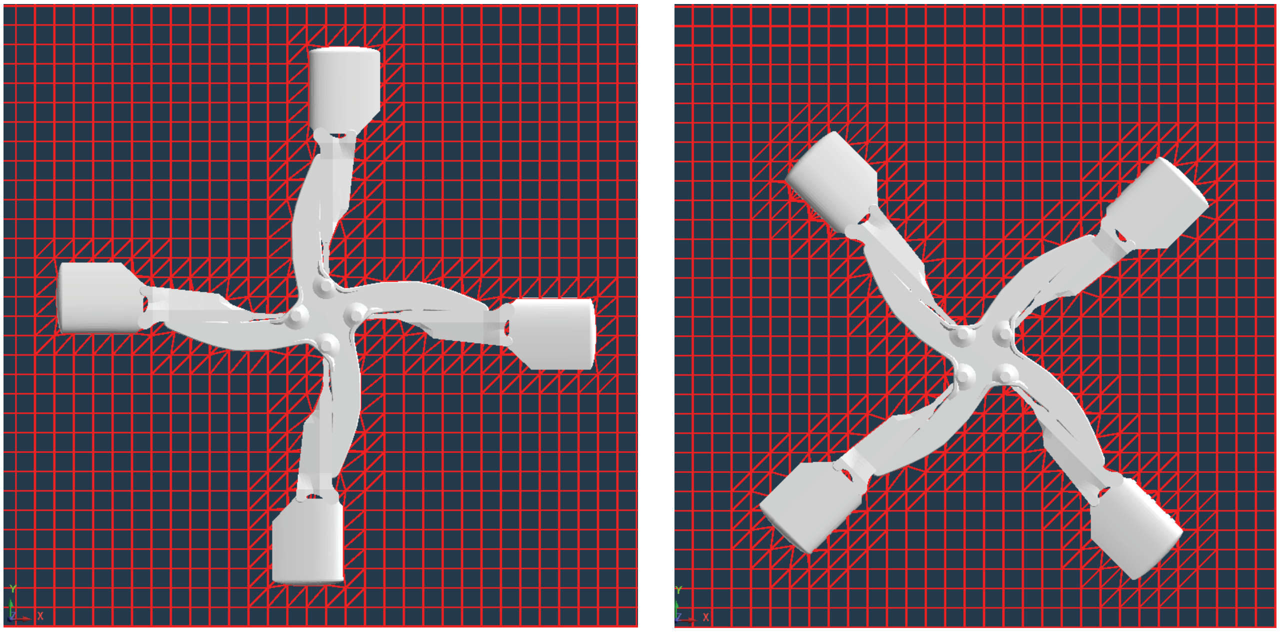

Figure 15: Side-by-side grid comparison of Configuration 4 rotated and nonrotated.

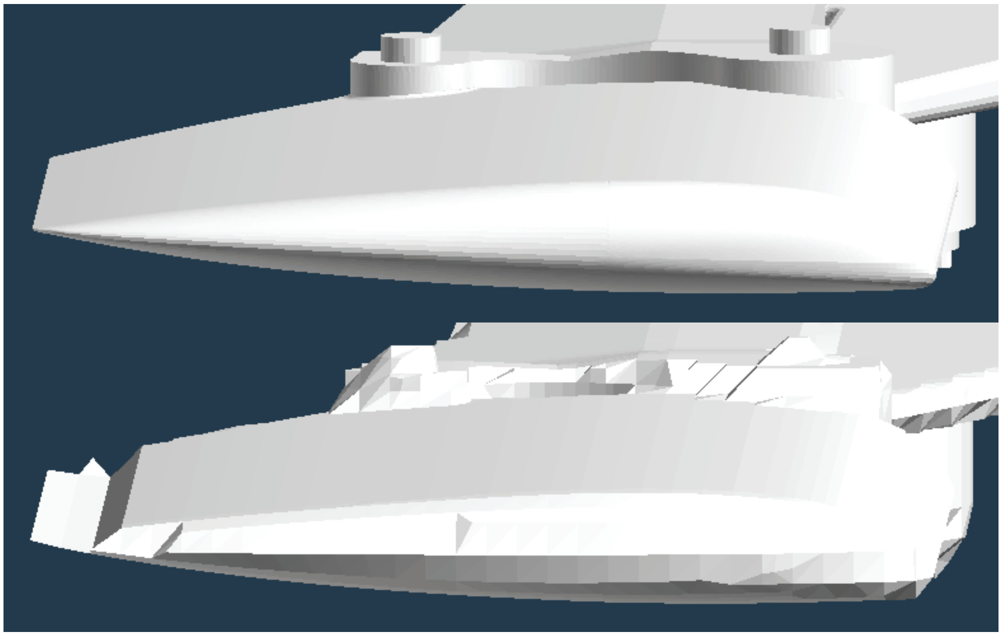

Figure 16: Comparison of the original geometry to the body generated by RotCFD.

Another interesting finding is that the predicted lift for all of the cases had significantly larger discrepancies than the predicted drag. This is a rather peculiar effect, as CFD is generally known to have more difficulty accurately predicting drag than lift. This effect is believed to be specific to the geometry as well. The hub geometry contains blade stubs that replaced full-length blades. These blade stubs were small compared to the entire geometry, and the trailing edges of the blade stubs were particularly thin compared to the surrounding cells. Figure 16 shows the original geometry compared to the generated body, which may have influenced the results.

The blades of a rotor are responsible for producing lift, and compromising the airfoil shape compromises the lift. It is therefore believed that the discrepancies in the lift predictions may be a result of the airfoil geometry approximation. The accuracy of the predicted pitching moment is also compromised as it is directly related to lift. When comparing the pitching moment data from the wind tunnel tests between Configurations 3 and 4, 6 and 7, and 8 and 9, it can be seen that the addition of the blade stubs has a large contribution to the pitching moment. Therefore, a conclusion can be drawn that small differences in lift values greatly impact the pitching moment values. Predicted drag remained relatively accurate, because the general shape of the airfoil was minimally distorted. Since the body is mostly blunt, a large portion of the drag will therefore be pressure drag and not viscous drag. Since RotCFD can cope better with pressure drag compared to viscous drag, this could be the reason for the relatively accurate and stable drag results obtained.

Increasing the body refinement would have resolved this issue and may have resulted in a significantly more accurate prediction in lift, pitching moment, and possibly drag as well. As drag was of much higher importance in this project, the limited accuracy of predicted lift and pitching moment can be tolerated, as long as predicted drag was accurate. Increasing the body refinement would have exponentially increased computational time and the timeframe of this project, therefore, body refinement was not increased.

An accurate simulation of Configuration 0 proved to be another challenge. Data for Configuration 0 was recorded during the wind tunnel tests in order to gather appropriate information to apply aerodynamic tares and calibrate the test runs. Obtaining accurate numbers for the simulation would validate RotUNS as an appropriate tool to model the wind tunnel tests for this project.

Multiple Configuration 0 cases were attempted with various spatial and time grids, but none of the cases matched the experimental data within the 10-percent margin of error. Greater detail of the Configuration 0 cases and results is shown in Appendix C. Nearly all of the simulations predicted drag numbers that were roughly half of the experimental value. The precision of the cases with similar results across multiple grids suggests that the simulation results are accurate for the configuration modeled. As a result, it is believed that there is a physical discrepancy between the simulation conditions and wind tunnel conditions.

Further inspection of the 7- by 10-foot wind tunnel floor revealed a feature of the wind tunnel that was not modeled. Figure 17 shows a picture of the additional space below the wind tunnel floor that surrounds the test stand. It is believed that this feature could have contributed to a large amount of the drag recorded in the experimental test run due to the extra flow path and likelihood of large amounts of stagnant air gathering in this region. These floor cavities were not modeled in the simulations and are most likely responsible for the offset of the predicted drag. In the interest of time, the floor geometry was not studied; however, further work on this project might include attempts to model this feature in RotCFD.

This issue also affected the cases that modeled wind tunnel conditions since they included the test stand. To overcome this issue, a separate force-moment group had to be created for the hub in RotCFD. This allowed the hub forces and moments to be calculated separately from the test stand. This results in another source of error as the flow near the bottom of the test stand is known to be inaccurate. However, it was assumed that the flow closer to the hub would remain relatively unchanged.

Aerodynamic tares had to be separately applied to the raw wind tunnel results to have directly comparable data. Predicted drag and lift values were consistently accurate across the free-stream condition and wind tunnel condition cases. However, predicted pitching moments are significantly more inaccurate for cases in wind tunnel conditions. This can be a byproduct of the altered flow resulting from inaccurately modeling the test stand.

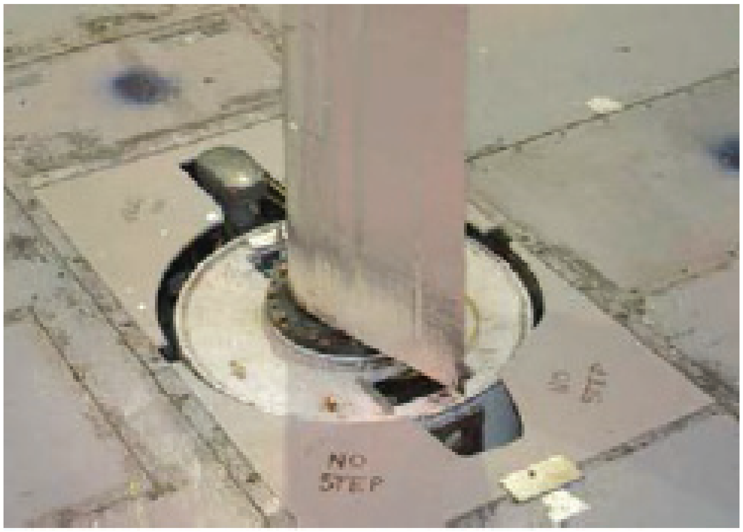

Figure 17: Picture of the floor cavities beside the test stand in the 7- by 10-foot wind tunnel [3].

Epsilon Residual Solution With Time

An issue was encountered when incorrect convergence time history behavior was observed for a particular case. Figure 18 shows the force and moment history for Configuration 6 with $\psi = 45°$, $\alpha_s = 6°$, and free-stream conditions. The drag, plotted in yellow, initially appears to converge to the proper solution at approximately 70 lb; however, at around 4,000 time steps, the drag increases and converges at a much larger value. This result was reproduced with a variety of spatial and time grids.

The error was attributed to a problem with the epsilon solution in the turbulence model. The solution file lists the epsilon residual as ‘infinity’ after the initial spike at 4,000 time steps. This signifies that the epsilon solution has diverged even though the flow solver itself has converged. A suggested recommendation is that the user should be notified that the turbulence solutions have diverged. It should be noted that laminar cases should not experience this issue and can be a viable alternative under conditions with minimal turbulence.

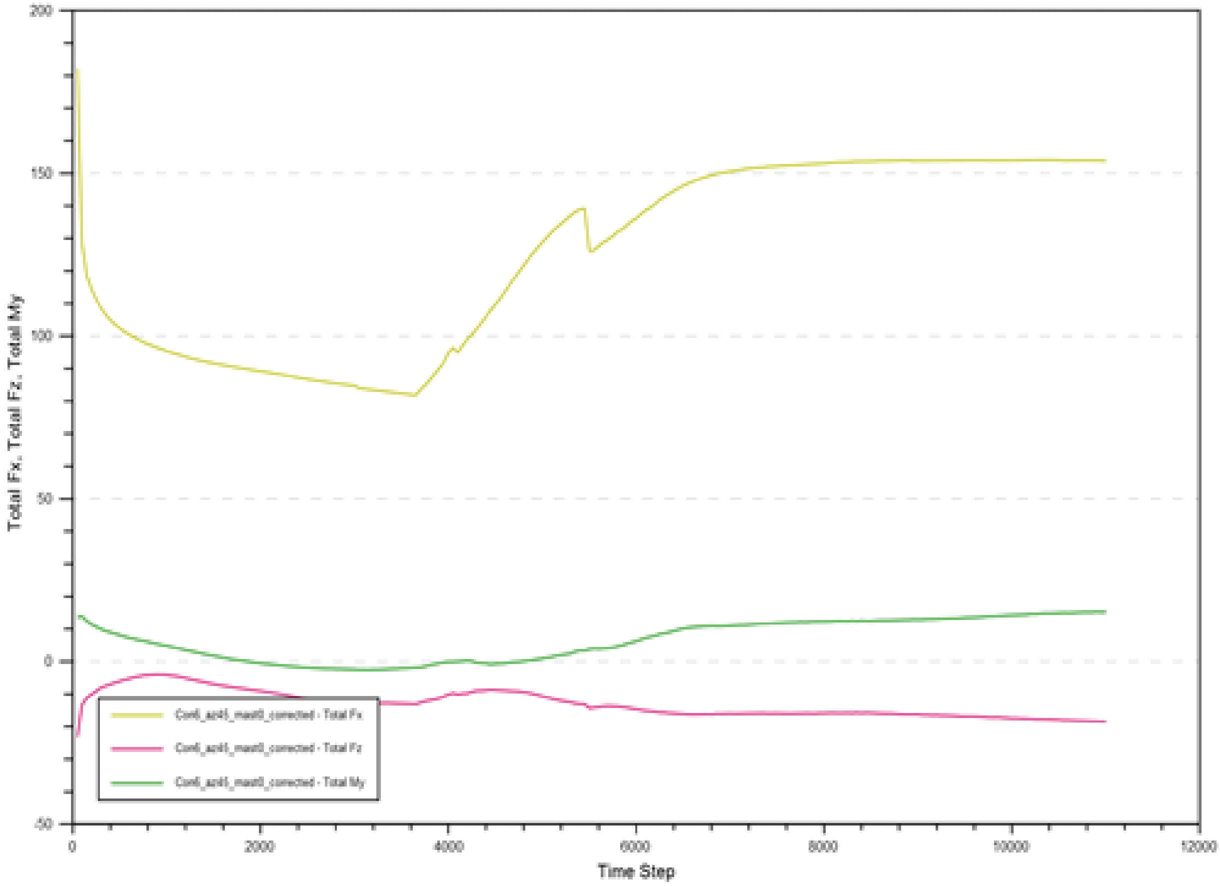

Figure 18: Force and moment history for Configuration 6 at $\psi = 45°$ and $\alpha_s = 6°$, modeled in free-stream conditions.

CONCLUSIONS

Testing was completed under the U.S. Army Aviation Development Directorate of a 2/5th scale AH-56 Cheyenne helicopter hub in multiple build-up configurations. Drag, lift, and pitching moment data were recorded for azimuthal and alpha sweeps. Using geometries created in Creo, Configurations 4, 6, and 8 were simulated using RotCFD. The selected configurations were run at $\psi = 0°$ and $45°$ and $\alpha_s = 0°$ and $45°$. After completing the simulations, the drag, lift, and pitching moment results were compared to the data obtained from the wind tunnel testing. The criterion for a successful case was matching the predicted drag to within 10 percent of the experimental data. With accurate simulation results, more geometries could be added to the hub for additional RotCFD testing rather than continuing wind tunnel testing, saving time and money.

Drag was accurately predicted to within the 10-percent acceptable limit for a total of 13 cases. Though some RotCFD bugs were discovered in the process of this work, it was determined to still be an accurate tool in evaluating hub performance under certain conditions. Corrections made to extrapolate wind tunnel results to free-stream conditions were also validated to a certain extent. It was found that a physical discrepancy between the model and the wind tunnel may have been a source of error in the calculations, as well as the approximation of the model geometry. Additionally, a recommendation is that the user should be notified that the turbulence solutions have diverged when using the OpenCL version of the solver.

APPENDIX A

CONFIGURATION INFORMATION

Config 1: Lower shaft only

Config 2: + fixed hub

Config 3: + blade grips

Config 4: + blade stubs

Config 5: + pitch horns

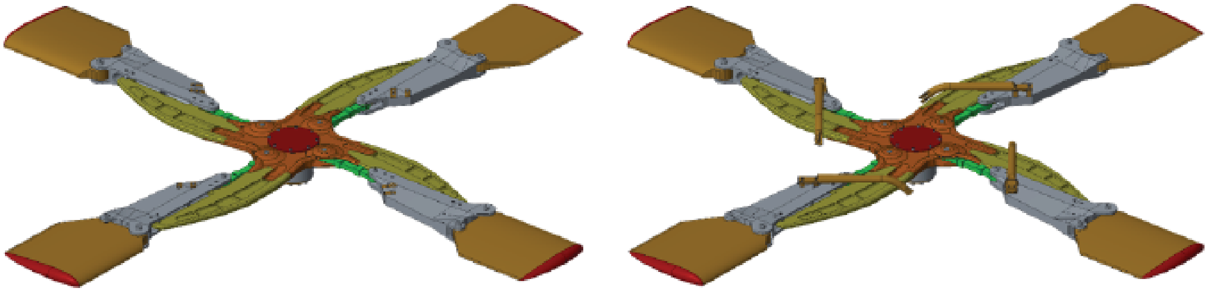

Config 6: + flight control gyro

Config 7: Config 6 - blade stubs

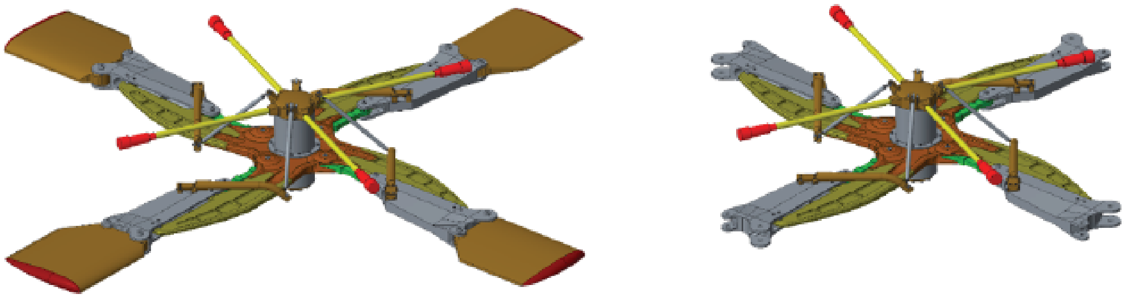

Config 8: Config 4 + fairing

Config 9: Config 8 – blade stubs

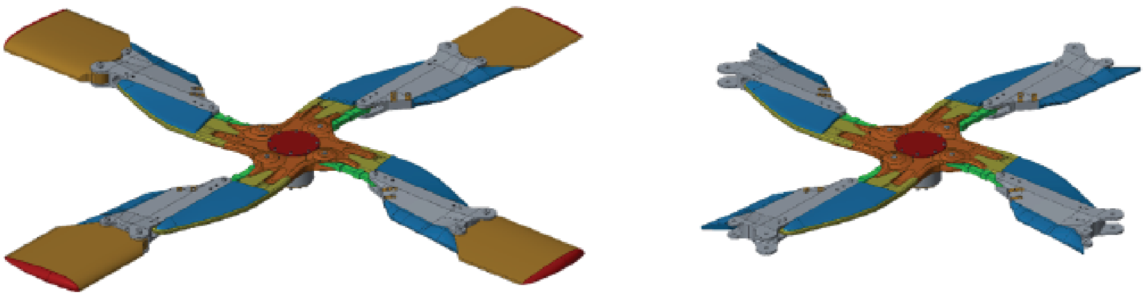

Figure A-1: All 9 build-up configurations tested in the 7- by 10-foot wind tunnel [1].

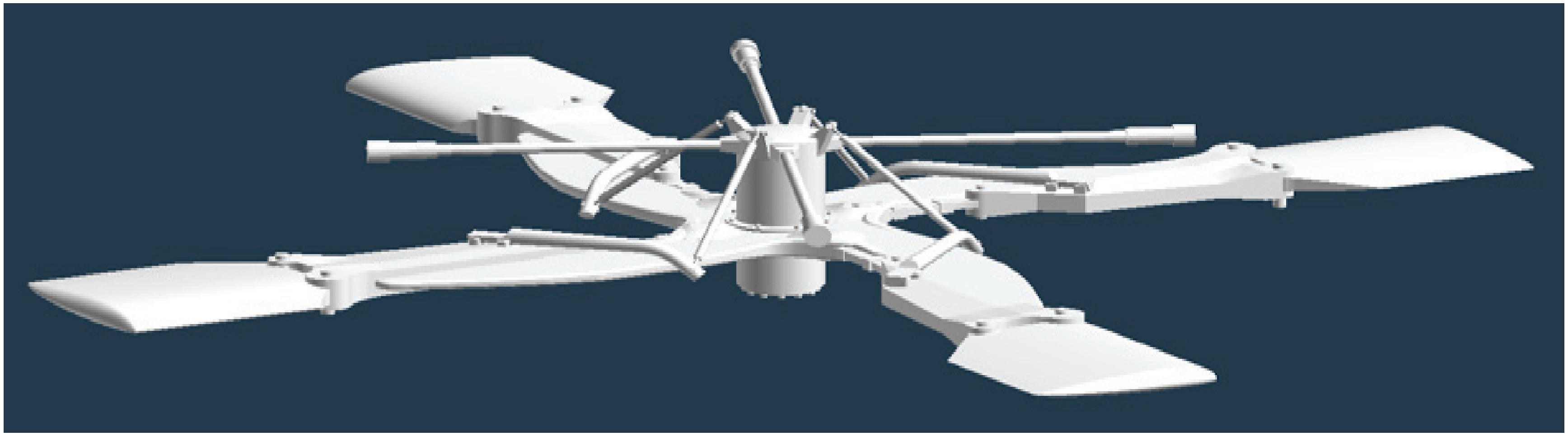

Figure A-2: Rhino file for Configuration 6 loaded into RotCFD.

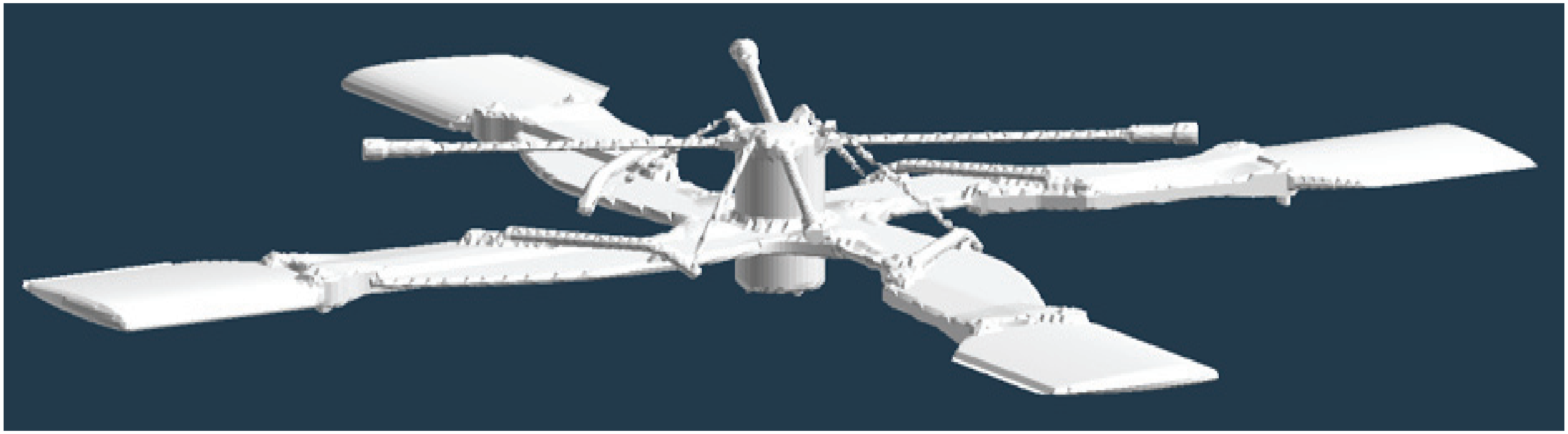

Figure A-3: View of how RotCFD views the geometry after gridding.

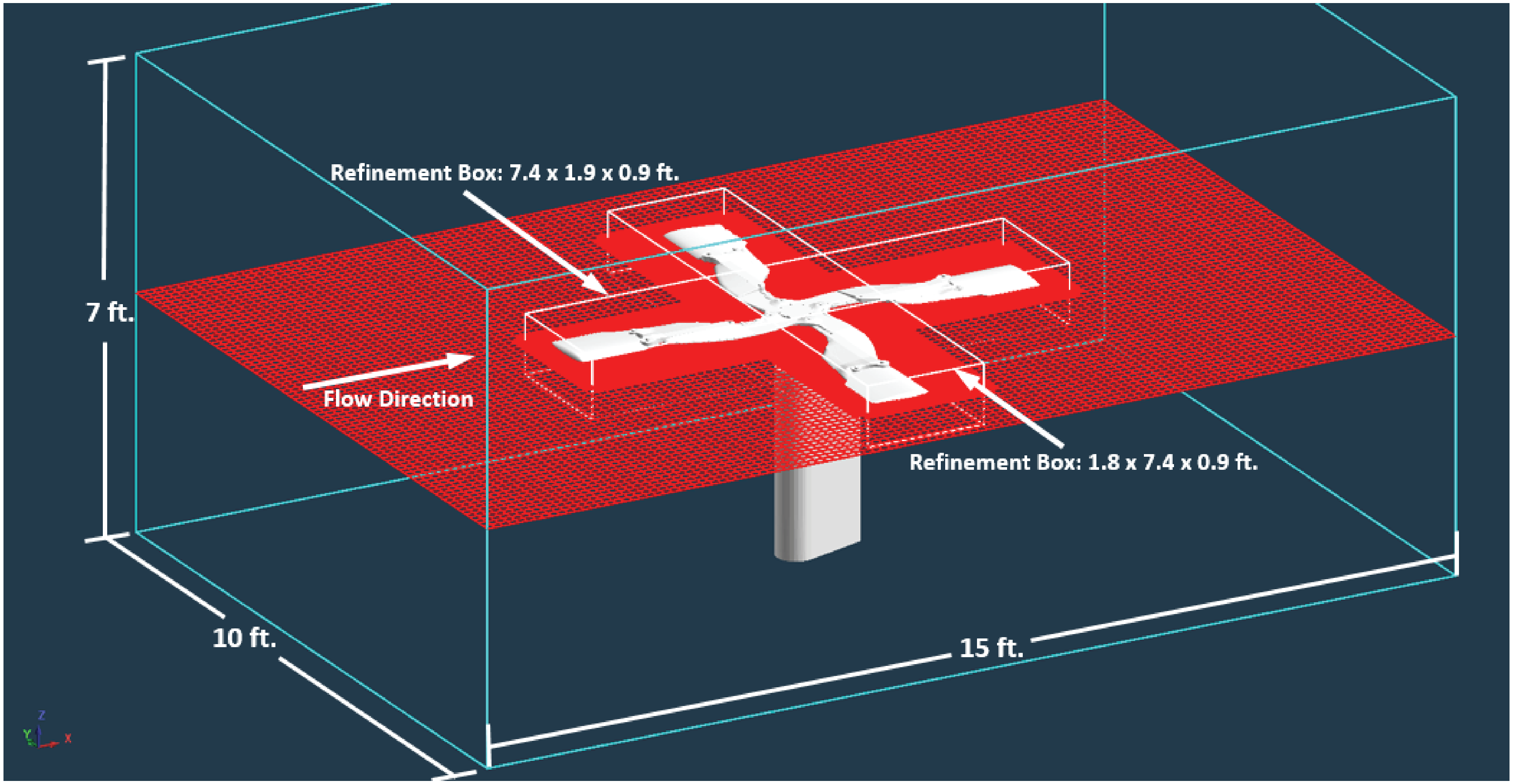

Figure A-4: Illustration of the RotCFD spatial grid set up for Configuration 4 in wind tunnel conditions.

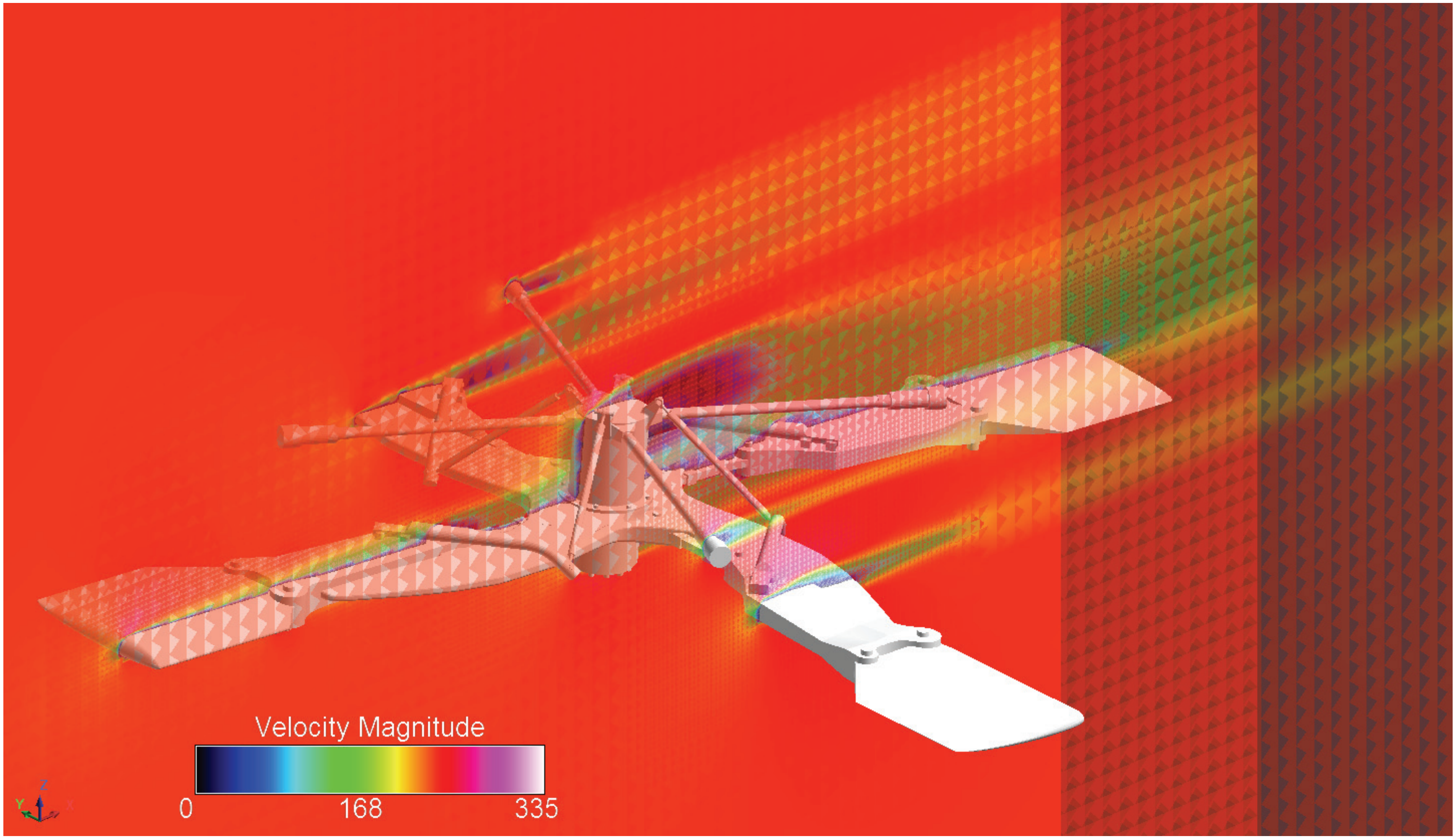

Figure A-5: Y-plane flow velocity magnitude through the center of the hub for Configuration 6 at ψ = 45° and α = 6°.

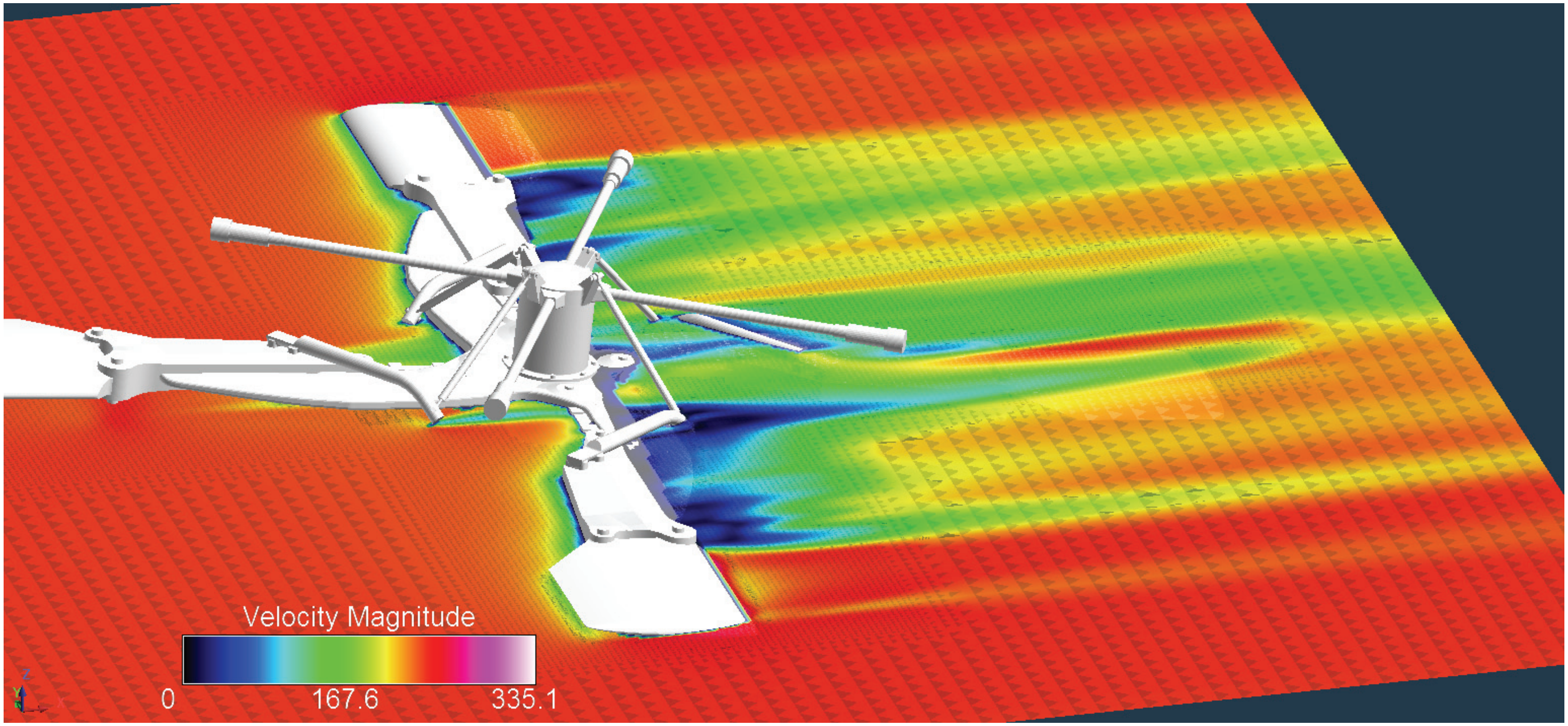

Figure A-6: Z-plane flow velocity magnitude through the center of the hub for Configuration 6 at ψ = 45° and α = 6°.

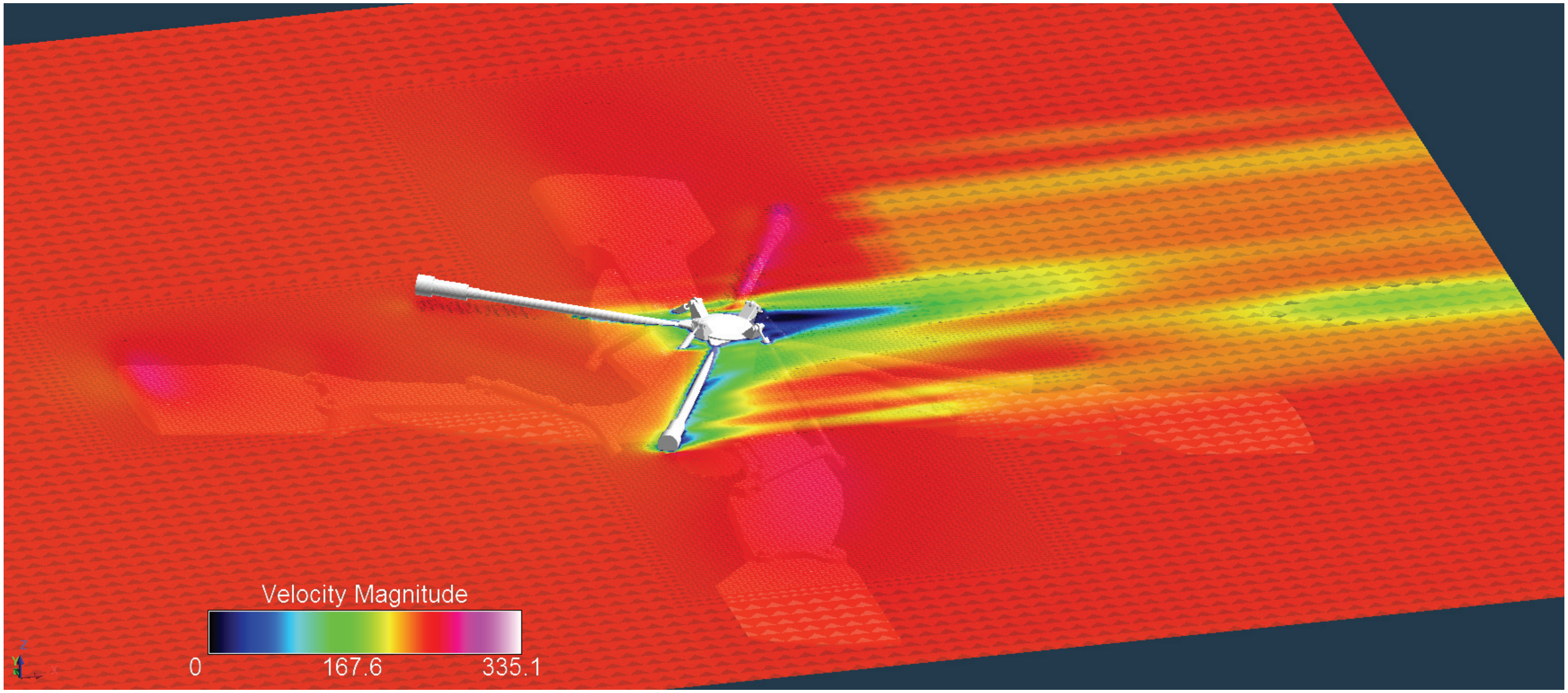

Figure A-7: Z-plane flow velocity magnitude through the mechanical control gyro for Configuration 6 at ψ = 45° and α = 6°.

APPENDIX B

AERODYNAMIC TARE COEFFICIENTS

Table B-1: Coefficients for Aerodynamic Tare [3].

	$\boldsymbol{P_1}$	$\boldsymbol{P_2}$	$\boldsymbol{P_3}$	$\boldsymbol{P_4}$
D	1.0696×10^{-2}	2.2233×10^{-2}	5.1744×10^{-1}	4.8684×10^{1}
L	3.2678×10^{-2}	3.2690×10^{-2}	5.6513×10^{-1}	2.7565×10^{1}
PM	-2.6925×10^{-2}	-1.7007	-1.1615×10^{2}	-

Coefficients for the aerodynamic tare polynomial are in the form of Equations 3, 4, and 5 below. Both D_{tare} and L_{tare} are in units of lb, PM_{tare} is in ft lbs, and $\alpha_{s,u}$ is in degrees.

$$D_{tare} = P_1\alpha_{s,u}^3 + P_2\alpha_{s,u}^2 + P_3\alpha_{s,u} + P_4 \tag{3}$$

$$L_{tare} = P_1\alpha_{s,u}^3 + P_2\alpha_{s,u}^2 + P_3\alpha_{s,u} + P_4 \tag{4}$$

$$PM_{tare} = P_1\alpha_{s,u}^2 + P_2\alpha_{s,u} + P_3 \tag{5}$$

APPENDIX C

UNCORRECTED SIMULATION GRID INFORMATION

Table C-1: Time grid information for completed RotCFD cases.

Configuration	Walls Condition	Azimuth Angle (deg)	Mast Angle (deg)	Time Grid		Walls Condition	Time Grid	
				Total Time (s)	Time Steps		Total Time (s)	Time Steps
4	0	0	Uncorrected	0.065	6500	Corrected	0.08	8000
				0.01	1000			
4	0	6	Uncorrected	0.01	3000	Corrected	0.01	3000
				0.04	8000		0.04	8000
4	45	0	Uncorrected	0.01	3000	Corrected	0.01	3000
				0.055	11000		0.04	8000
4	45	6	Uncorrected			Corrected	0.01	3000 (13 iterations)
							0.04	8000 (12 iterations)
6	0	0	Uncorrected			Corrected	0.05	5000
6	0	6	Uncorrected			Corrected	0.01	3000
							0.04	8000
6	45	0	Uncorrected			Corrected	0.01	6000
							0.01	16000
							0.03	12000
6	45	6	Uncorrected			Corrected	.05	15000
8	0	0	Uncorrected	0.05	5000	Corrected	0.05	5000
				0.015	1500		0.01	1000
8	0	6	Uncorrected			Corrected	0.04	8000
8	45	0	Uncorrected	0.01	3000	Corrected	0.01	3000
				0.055	11000		0.04	8000
8	45	6	Uncorrected			Corrected		Unfinished

Note: All cases were run with 10 iterations per time step unless otherwise noted

Table C-2: Computer Specifications.

Wind Velocity	Configuration	Wall Condition	Azimuth	Mast Angle	Cell Count	Total Iterations	Run Time (hours)	GPU CUDA Cores	RAM (GB)	CPU Threads
225.4	4	Uncorrected	0	0	1,683,942	75,000	36*	640	32	4
225.3	4	Uncorrected	0	6	1,901,076	110,000	54.5	640	8	4
225	4	Uncorrected	45	0	1,963,680	140,000	141	1536	32	24
230	4	Corrected	0	0	1,571,507	80,000	38*	640	8	4
230	4	Corrected	0	6	1,788,476	135,000	52	640	32	4
230	4	Corrected	45	0	2,026,476	110,000	67	640	8	4
230	4	Corrected	45	6	2,408,818	135,000	N/A†	640	8	4
230	6	Corrected	0	0	1,848,154	5,000	41	2048	32	32
230	6	Corrected	0	6	1,829,783	110,000	116.4	1536	32	24
230	6	Corrected	45	0	1,103,258	340,000	48.5*	2048	32	32
230	6	Corrected	45	6	2,033,195	150,000	226.5‡*	1536	32	24
227.1	8	Uncorrected	0	0	1,772,801	65,000	N/A†	640	32	4
230	8	Corrected	0	0	1,589,743	60,000	26	640	16	4
230	8	Corrected	0	6	1,766,628	110,000	57.9	640	8	4
230	8	Corrected	45	0	1,921,664	110,000	56.5	640	16	4
230	8	Corrected	45	6		Unfinished				

Note: All cases were run on GPUs with single precision unless otherwise specified.

*Run times that were estimated from restart files.
†Run times that were lost due to restart files.
‡Run on GPU with double precision.

Table C-3: Time grid information for Configuration 6, $\psi = 45°$, $\alpha_s = 6°$, case study.

Trial	Total Time (s)	Time Steps	Iterations per Time Step	Relaxation Factor (u, v, w, p)	Diverged at Time Step	Diverged at Approx. Time (s)
1	0.050	5000	10	0.10	4	0.00004
2	0.050	8000	10	0.10	1000	0.006
3	0.050	10000	10	0.10	1200	0.006
4	0.010	3000	10	0.10	1800	0.006
	0.040	8000	10	0.10		
5	0.010	3000	8	0.10	2000	0.006
	0.040	8000	8	0.10		
6	0.050	15000	10	0.10	1850	0.006
7	0.050	20000	10	0.10	2400	0.006
8	0.043	7000	9	0.10	1000	0.006
9	0.008	1500	10	0.05	1450	0.007
	0.007	1400	10	0.06		
	0.007	1400	10	0.07		
	0.007	1400	10	0.08		
	0.007	1400	10	0.09		
	0.007	1400	10	0.10		
10	0.005	1000	10	0.10	1375	0.007
	0.002	400	10	0.01		
	0.038	7600	10	0.10		
11	0.050	15000	10	0.10	5200	0.0173

Table C-4: Spatial grid information for Configuration 6, $\psi = 45^\circ$, $\alpha_s = 6^\circ$, case study.

Trials 1–10								
Boundary		Grid Specs	Re. Box 1	Re. Box 2	Re. Box 3	Re. Box 4	Re. Box 5	Re. Box 6
–5.00	Walls	10	–5.00	0.00	–1.40	–1.40	–2.70	–2.50
–5.00	X-min: Velocity	10	–5.00	–3.10	–1.90	–1.80	–2.80	1.30
–1.50	X-max: mass output correction	10	–1.50	3.60	3.60	3.30	3.40	3.40
5.00	Others: Velocity	6	5.00	3.50	2.40	0.00	–0.90	–0.70
5.00		(fit bodies) checked	5.00	2.90	2.00	2.00	–1.00	3.10
8.50			8.50	2.90	4.30	3.60	4.00	4.00
			4	6	6	6	6	6

Trial 11								
Boundary		Grid Specs	Re. Box 1	Re. Box 2	Re. Box 3	Re. Box 4	Re. Box 5	Re. Box 6
–5.01	Walls	10	–5.01	0.00	–1.40	–1.40	–2.70	–2.50
–5.01	X-min: Velocity	10	–5.01	–3.10	–1.90	–1.80	–2.80	1.30
–1.51	X-max: mass out	10	–1.51	3.60	3.60	3.30	3.40	3.40
5.01	Others: Velocity	6	5.01	3.90	2.40	0.00	–0.90	–0.70
5.01		(fit bodies) checked	5.01	2.90	2.00	2.00	–1.00	3.10
8.51			8.51	2.90	4.30	3.60	4.00	4.00
			4	6	6	6	6	6

Table C-5: Configuration 0 (mast-only) case study.

Trial	Flow Velocity (ft/s)	Body Refinement	Boundary Box Refinement	Refinement Box	Drag (lb)	Lift (lb)	Moment (lb-ft)
Wind Tunnel	225.0	-	-	-	48.8	27.6	–116.4
1	230.0	6	3	4	30.0	13.0	–55.0
2	230.0	6	3	5	26.0	13.0	–51.0
3	230.0	6	4	5	25.0	13.0	–48.0
4	230.0	6	4	5	25.0	13.0	–48.0
5	230.0	6	4	6	22.0	12.0	–39.0
6	157.9	6	4	6	10.5	6.0	–19.0

Trial 4 is the same as Trial 3, except it has an extended refinement box to more accurately capture the wake. In all cases the drag is approximately 40–55 percent low and the lift is approximately 55 percent low. Pitching moment is approximately 58 percent low.

APPENDIX D

CORRECTED SIMULATION GRID INFORMATION

Spatial Grid Information for Successful Corrected Cases

Table D-1: Spatial grid information for Configuration 4 at $\psi = 0°$ and $\alpha = 0°$.

	Grid Specs		Moment Point		Boundary	Re. Box 1	Re. Box 2	Re. Box 3
x cells	10	x	0	x-min	–5	–5	–3.7	–0.9
y cells	10	y	0	y-min	–5	–5	–1	–3.7
z cells	10	z	3.5	z-min	–1.5	–1.5	3.9	3
				x-max	5	5	3.7	0.9
				y-max	5	5	0.9	3.7
				z-max	8.5	8.5	3	3.9
					Refinement	4	6	6

Table D-2: Spatial grid information for Configuration 4 at $\psi = 0°$ and $\alpha = 6°$.

	Grid Specs		Moment Point		Boundary	Re. Box 1	Re. Box 2	Re. Box 3
x cells	10	x	0.36585	x-min	–5	–5	–3.4	–0.6
y cells	10	y	0	y-min	–5	–5	–1	–3.7
z cells	10	z	3.4808	z-min	–1.5	–1.5	4.2	3.1
				x-max	5	5	4	1.3
				y-max	5	5	0.9	3.7
				z-max	8.5	8.5	2.9	4
					Refinement	4	6	6

Table D-3: Spatial grid information for Configuration 4 at $\psi = 45°$ and $\alpha = 0°$.

	Grid Specs		Moment Point		Boundary	Re. Box 1	Re. Box 2	Re. Box 3
x cells	10	x	0	x-min	–5	–5	–3.1	–0.5
y cells	10	y	0	y-min	–5	–5	–3.2	–0.5
z cells	10	z	3.5	z-min	–1.5	–1.5	3.9	3.05
				x-max	5	5	3.5	0.5
				y-max	5	5	3.3	0.5
				z-max	8.5	8.5	3.1	3.1
					Refinement	4	6	6

Table D-4: Spatial grid information for Configuration 4 at $\psi = 45°$ and $\alpha = 6°$.

	Grid Specs		Moment Point		Boundary	Re. Box 1	Re. Box 2
x cells	10	x	0.36585	x-min	–5	–5	–3.2
y cells	10	y	0	y-min	–5	–5	–3.2
z cells	10	z	3.4808	z-min	–1.5	–1.5	4.1
				x-max	5	5	3.6
				y-max	5	5	3.3
				z-max	8.5	8.5	2.8
					Refinement	3	6

Table D-5: Spatial grid information for Configuration 6 at $\psi = 0°$ and $\alpha = 0°$.

	Grid Specs		Moment Point		Boundary	Re. Box 1	Re. Box 2	Re. Box 3
x cells	15	x	0	x-min	–5	–5	–3.7	–0.9
y cells	10	y	0	y-min	–5	–5	–1.2	–3.7
z cells	7	z	3.5	z-min	–1.5	–1.5	4.2	3.1
				x-max	5	5	3.7	0.9
				y-max	5	5	0.9	3.7
				z-max	8.5	8.5	3.1	4.2
					Refinement	4	6	6

Table D-6: Spatial grid information for Configuration 6 at $\psi = 0°$ and $\alpha = 6°$.

	Grid Specs		Moment Point		Boundary	Re. Box 1	Re. Box 2	Re. Box 3	Re. Box 4	Re. Box 5	Re. Box 6
x cells	10	x	0.36585	x-min	–5	–5	–3.4	–0.6	–3.4	–1.4	1.4
y cells	10	y	0	y-min	–5	–5	–1	–3.7	–0.8	0.3	–1
z cells	10	z	3.4808	z-min	–1.5	–1.5	4.2	3.1	3.4	4.1	3.6
				x-max	5	5	4	1.3	–0.7	–0.7	2.2
				y-max	5	5	0.9	3.7	1	1	–0.3
				z-max	8.5	8.5	2.9	4	4.1	4.3	4
					Refinement	4	6	6	6	6	6

Table D-7: Spatial grid information for Configuration 6 at $\psi = 45^\circ$ and $\alpha = 0^\circ$.

	Grid Specs		Moment Point		Boundary	Re. Box 1	Re. Box 2	Re. Box 3
x cells	10	x	0	x-min	–5	–5	–2.3	–1.8
y cells	10	y	0	y-min	–5	–5	–3.1	–1.9
z cells	10	z	3.5	z-min	–1.5	–1.5	3	3.9
				x-max	5	5	3.4	1.9
				y-max	5	5	3.1	1.9
				z-max	8.5	8.5	3.9	4.3
					Refinement	4	5	5

Table D-8: Spatial grid information for Configuration 6 at $\psi = 45^\circ$ and $\alpha = 6^\circ$.

	Grid Specs		Moment Point		Boundary	Re. Box 1	Re. Box 2	Re. Box 3	Re. Box 4	Re. Box 5	Re. Box 6
x cells	10	x	0.36585	x-min	–5	–5	0	–1.4	–2.7	–2.5	–1.4
y cells	10	y	0	y-min	–5	–5	–3.1	–1.9	–2.8	1.3	–1.9
z cells	10	z	3.4808	z-min	–1.5	–1.5	3.6	3.6	3.4	3.4	3.3
				x-max	5	5	3.9	3	–0.9	–0.7	0
				y-max	5	5	2.9	2	–1	3.1	2
				z-max	8.5	8.5	2.9	4.3	4	4	3.6
					Refinement	4	6	6	6	6	6

Table D-9: Spatial grid information for Configuration 8 at $\psi = 0^\circ$ and $\alpha = 0^\circ$.

	Grid Specs		Moment Point		Boundary	Re. Box 1	Re. Box 2	Re. Box 3
x cells	10	x	0	x-min	–5	–5	–3.7	–0.9
y cells	10	y	0	y-min	–5	–5	–1	–3.7
z cells	10	z	3.5	z-min	–1.5	–1.5	3.9	3
				x-max	5	5	3.7	0.9
				y-max	5	5	0.9	3.7
				z-max	8.5	8.5	3	3.9
					Refinement	4	6	6

Table D-10: Spatial grid information for Configuration 8 at $\psi = 0°$ and $\alpha = 6°$.

	Grid Specs		Moment Point		Boundary	Re. Box 1	Re. Box 2	Re. Box 3
x cells	10	x	0.36585	x-min	–5	–5	–3.6	–6
y cells	10	y	0	y-min	–5	–5	–1	–3.7
z cells	10	z	3.4808	z-min	–1.5	–1.5	4.1	3.1
				x-max	5	5	4.2	1.3
				y-max	5	5	0.9	3.7
				z-max	8.5	8.5	2.9	4
					Refinement	4	6	6

Table D-11: Spatial grid information for Configuration 8 at $\psi = 45°$ and $\alpha = 0°$.

	Grid Specs		Moment Point		Boundary	Re. Box 1	Re. Box 2
x cells	10	x	0	x-min	–5	–5	–3
y cells	10	y	0	y-min	–5	–5	–3
z cells	10	z	3.5	z-min	–1.5	–1.5	3
				x-max	5	5	3
				y-max	5	5	3
				z-max	8.5	8.5	3.8
					Refinement	4	6

Table D-12: Spatial grid information for Configuration 8 at $\psi = 45°$ and $\alpha = 6°$.

	Grid Specs		Moment Point		Boundary	Re. Box 1	Re. Box 2	Re. Box 3
x cells	10	x	0.36585	x-min	–5	–5	N/A	N/A
y cells	10	y	0	y-min	–5	–5	N/A	N/A
z cells	10	z	3.4808	z-min	–1.5	–1.5	N/A	N/A
				x-max	5	5	N/A	N/A
				y-max	5	5	N/A	N/A
				z-max	8.5	8.5	N/A	N/A
					Refinement	4	6	6

Note: All corrected cases were run with free-stream walls, body refinement of 6, and fit-bodies.

Spatial Grid Information for Successful Uncorrected Cases

Table D-13: Spatial grid information for Configuration 4 at $\psi = 0°$ and $\alpha = 0°$.

	Grid Specs		Moment Point		Boundary	Re. Box 1	Re. Box 2	Re. Box 3
x cells	15	x	0	x-min	–7.5	–7.5	–3.7	–0.9
y cells	10	y	0	y-min	–5	–5	–1	–3.7
z cells	7	z	3.5	z-min	0	0	3.9	3
				x-max	7.5	7.5	3.7	0.9
				y-max	5	5	0.9	3.7
				z-max	7	7	3	3.9
					Refinement	4	6	6

Table D-14: Spatial grid information for Configuration 4 at $\psi = 0°$ and $\alpha = 6°$.

	Grid Specs		Moment Point		Boundary	Re. Box 1	Re. Box 2	Re. Box 3
x cells	15	x	0.36585	x-min	–7.5	–7.5	–0.6	–3.4
y cells	10	y	0	y-min	–5	–5	–3.7	–1
z cells	7	z	3.4808	z-min	0	0	3	4
				x-max	7.5	7.5	1.3	4.1
				y-max	5	5	3.7	0.9
				z-max	7	7	3.8	2.8
					Refinement	4	6	6

Table D-15: Spatial grid information for Configuration 4 at $\psi = 45°$ and $\alpha = 0°$.

	Grid Specs		Moment Point		Boundary	Re. Box 1	Re. Box 2	Re. Box 3
x cells	15	x	0	x-min	–7.5	–7.5	–3.2	–0.5
y cells	10	y	0	y-min	–5	–5	–3.1	–0.5
z cells	7	z	3.5	z-min	0	0	3.85	3
				x-max	7.5	7.5	3.4	0.5
				y-max	5	5	3.1	0.5
				z-max	7	7	3.15	3.15
					Refinement	4	6	6

Table D-16: Spatial grid information for Configuration 8 at $\psi = 0°$ and $\alpha = 0°$.

	Grid Specs		Moment Point		Boundary	Re. Box 1	Re. Box 2	Re. Box 3
x cells	15	x	0	x-min	–7.5	–7.5	–3.7	–0.9
y cells	10	y	0	y-min	–5	–5	–1	–3.7
z cells	7	z	3.5	z-min	0	0	3.9	3
				x-max	7.5	7.5	3.7	0.9
				y-max	5	5	0.9	3.7
				z-max	7	7	3	3.9
					Refinement	4	6	6

Note: All uncorrected cases were run with viscous walls, body refinement of 6, and fit-bodies.

REFERENCES

[1] Vocke, R. and Nunez, G.: Test Data Report, Low-Speed Wind Tunnel Drag Test of a 2/5 Scale Lockheed AH-56 Cheyenne Door-Hinge Hub. U.S. Army Aviation Development Directorate RDMR-AD-16-03, Mountain View, CA, 2016.

[2] Grima, A.: Aerodynamic Characterisation of an Experimental Tilt-Wing Aircraft. NASA Ames Research Center, Moffett Field, CA, 2016.

[3] Rajagopalan, R. G.; Baskaran, V.; Hollingsworth, A.; Lestari, A.; Garrick, D.; Solis, E.; and Hagerty, B.: RotCFD—A Tool for Aerodynamic Interference of Rotors: Validation and Capabilities. American Helicopter Society Future Vertical Lift Aircraft Design Conference, San Francisco, CA, 2012.

[4] Thorell, N. L.; Poux, A. M.; Syed, M. A.; and Maser, S. N.: RotCFD: UNS2D Airfoils Report. NASA Ames Research Center, Moffett Field, CA, 2015.

[5] Johnson, J. N.; Bender, G. L.; McClellan, R. D.; Burden, J. R.; and Larson, M. E.: Attack Helicopter Evaluation AH-56 Cheyenne Compound Helicopter. National Technical Information Service, Alexandria, VA, 1972.